

Responses to Anonymous Referee #1

This paper used WRF-Chem model to explore the feedback mechanisms of BB aerosols-climate interactions during March biomass burning in Indochina Peninsula. They reported that BB released aerosols could inhibit precipitation in ICP, showing instant and lag effects on local and regional rainfall. To discern the feedback effects, authors conducted two groups of simulations with control (CTRL) and sensitivity (BBER) model scenario experiments. They then compared the results from CTRL and BBER to quantify the BB effects.

Responses: We greatly appreciate these comments and suggestions. The manuscript has been improved by considering these comments and suggestions. Our detail responses are given point by point below in blue. The revised text is highlighted in red.

The paper is well-written and result analysis makes sense. My concern is that WRF-Chem modeling system fully coupled with two-way interaction offers unique option to examine the association between aerosols and meteorology. The feedback configuration takes into account both direct and indirect aerosol effects, thereby to provide better interpretations to the feedback effects on meteorology by turning on and off the feedback configuration. Authors' modeling investigation rely largely on the selection of BB emission reduction or enhancement in the sensitivity experiment.

Responses: As mentioned by the reviewer, aerosol climate effects can also be examined using the WRF-Chem model by turning on and off the feedback configuration, as in previous studies (e.g., Ding et al., 2021; Wang et al., 2021). However, emission perturbations have also been widely used in BB aerosol climate effect modelling studies apart from switching feedback processes. For instance, both Lee and Wang (2020) and Takeishi and Wang (2022) investigated the impacts of BB aerosols over the Maritime Continent based on their WRF-Chem experiments with and without BB emissions. Similarly, Lee et al. (2014), Dong et al. (2019) and Chavan et al. (2021) used this approach to study the BB aerosols' impacts on climate over the Indochina Peninsula (ICP). Thornhill et al. (2018) compared two simulations with the highest and lowest observed BB emissions in South America during 1997–2011. Yang et al. (2022) characterized the effects of BB aerosols by using the difference between the simulation with double ($\times 2$) BB emission and that with controlled ($\times 1$) BB emission. Liu et al.

(2020a) designed a complex series of experiments that included both four BB emission scenarios and turning-on and -off aerosol radiation feedback, in order to examine the relative importance of aerosol-cloud interactions (ACIs) and aerosol-radiation interactions (ARIs) over the Amazon.

Nevertheless, as concerned by the reviewer, we also ran an additional case same as CTRL, except that aerosol-climate feedbacks (both ARIs and ACIs) were turned off (labelled as Non-Feedback; only one member starting on February 25th 2010). As shown in Figure R1, the anomalous patterns of precipitation and 850-hPa wind from these two methods are quite similar, confirming that our method of reducing BB emission in this study is reliable. Note that the precipitation and 850-hPa wind anomalies from the Non-Feedback run are somewhat greater than those from BBER. This may be because 100% of the total BB aerosols are considered in the Non-Feedback run (their ACIs and ARIs were turned off), while only 85% of the total BB aerosols are considered in the differences between CTRL and BBER (i.e., CTRL minus BBER). It should also be noted that we only turned off the ACIs and ARIs from all anthropogenic aerosols (including BB aerosols) in the Non-feedback run, but the similar anomaly patterns from the BBER and Non-Feedback runs at least confirm that our results are reliable and further suggest that the effect of BB aerosols dominates in the BB season over the ICP, while other anthropogenic aerosols might only play a minor role. Overall, we believe that results should be similar based on these two simulating approaches.

To simplify the process, we reduced the BB emission to 15% in the BBER run because the BB emission over the ICP in 2001, the year with the lowest BB emission during 1998–2019, is about one-sixth of that in 2010. This would be more realistic. Nevertheless, the BB emission reduction rate in the sensitivity experiment may also affect our results. Thus, we also ran another test with half BB emission (Half; only one member starting on February 25th 2010). As shown in Figure R2, the differences in precipitation and 850-hPa wind of the two BB emission reduction scenarios with respect to CTRL are quite similar in pattern but with different magnitude. For example, the rainfall anomalies are 72.73%, 36.15% and 31.50% of that from BBER in March, early- and mid-April, respectively. This indicates that our qualitative conclusions are robust. We understand that the responses of atmospheric circulation and precipitation to aerosols are not linear with increasing aerosol loading (Liu et al., 2020a). Thus, we plan to quantify the climate responses to BB emission by designing different emission

scenarios over the ICP in the future.

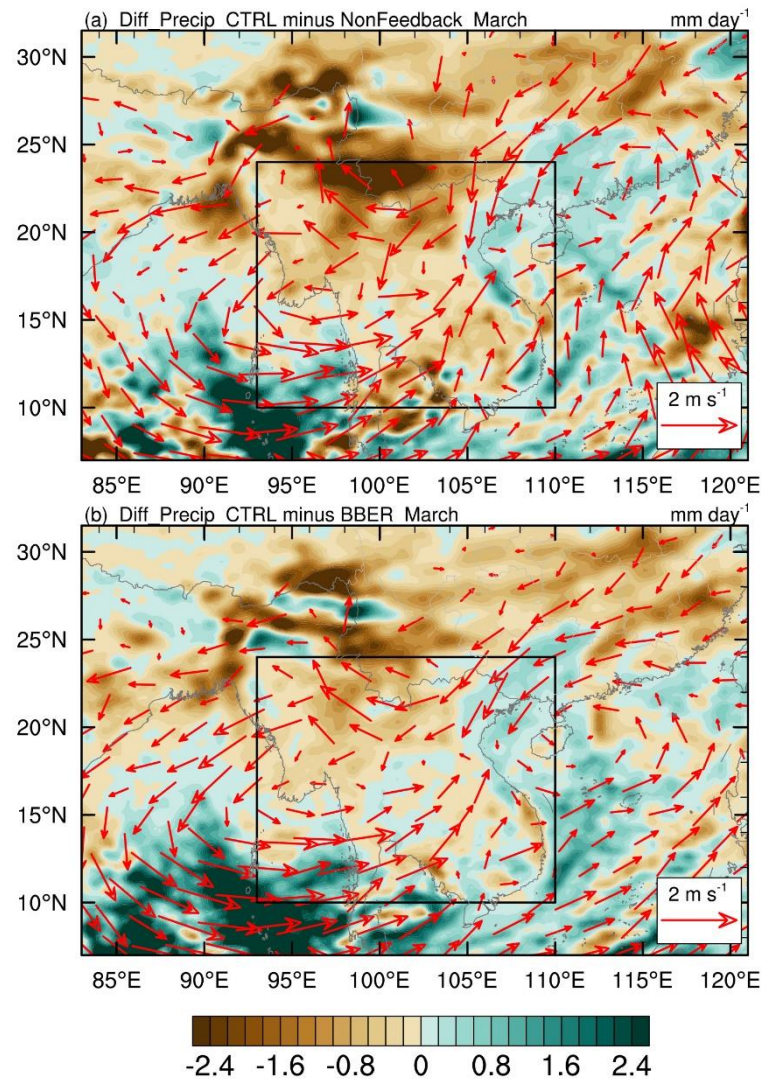


Figure R1: Comparison of model simulations with different model settings. (a) The differences in precipitation (shading; mm day⁻¹) and 850-hPa wind (vector; m s⁻¹) between CTRL and Non-Feedback (i.e., CTRL minus Non-Feedback) during March of 2010. (b) Same as (a), but for the differences between CTRL and BBER (i.e., CTRL minus BBER). Note that both CTRL and BBER runs here contain only one member of the ensemble runs, which started on February 25th 2010.

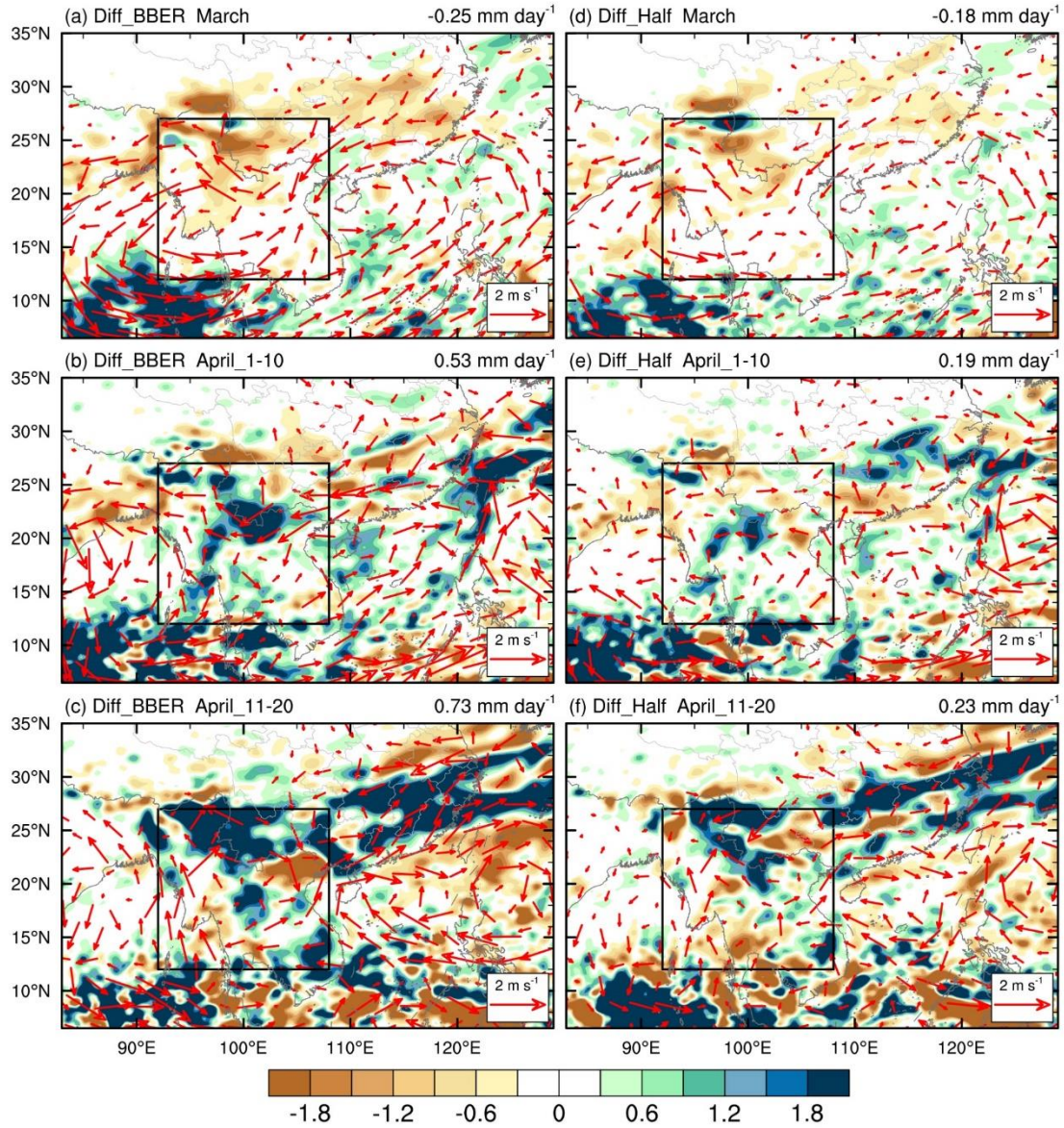


Figure R2: Comparison of model simulations with different BB emission reduction scenarios. (a–c) The differences in precipitation (shading; mm day⁻¹) and 850-hPa wind (vector; m s⁻¹) between CTRL and BBER (i.e., CTRL minus BBER) during (a) March, (b) early-April and (c) mid-April of 2010. (d–f) Same as (a–c) but for the differences between CTRL and Half (i.e., CTRL minus Half). The black box outlines the main region of precipitation anomalies in the ICP (92°–108°E, 12°–27°N), and the regional mean is given at the top-left corner of each panel. Note that the CTRL and BBER runs here have only one member of the ensemble runs, which started on February 25th 2010.

To state more clearly about our experimental design, we have revised the relevant statements around Page-9, Lines 167–170 in the revised manuscript to the following: “We chose the year of 2010 for modeling because the BB emission in 2010 was *greater than its climatology by about 1.7 standard deviations*. We reduced BB emission to 15%

as the sensitivity experiment in this study, because the March BB emission over the ICP in 2001, the year with the lowest BB emission during 1998–2019, is roughly 15% of that in 2010. It would be more realistic to investigate the effects of BB aerosols on atmospheric circulation and precipitation on the interannual timescale.”

In response to this comment, the following text has been added to the conclusions and discussion section (Page-29, Lines 539–550): *“It is worth noting that this study examines the BB aerosol climate effects using the model by reducing BB emission, while another method is commonly used, namely, by turning on and off the aerosol climate feedback configuration (e.g., Ding et al., 2021; Wang et al., 2021). We have done a simple verification, and found that the results obtained by the two methods are similar (Fig. S2). Additionally, although some quantitative results can be derived in this study, such as a 12.94(±4.22)% reduction (the value after “±” is a single standard deviation, hereafter the same) in rainfall in the ICP (92°–108°E, 12°–27°N) due to March BB aerosols’ instant effect, and 15.40(±5.11)% and 13.93(±5.65)% enhancements from the delayed effect in early- and mid-April, respectively, these quantitative results would rely on the BB emission reduction rate in the sensitivity experiment. A supplementary sensitivity test with 50% BB emission showed that the anomalous patterns of 850-hPa wind and rainfall are quite similar to those from BBER, but the rainfall anomalies are 72.73%, 36.15% and 31.50% of those from BBER in March, early- and mid-April, respectively (Fig. S3), indicating our qualitative conclusions are robust. As for quantitative results, this study is based on preliminary analysis; more experiments with different BB emission scenarios need to be designed to obtain more precise results in the future.”*

Can authors provide a BB emission map in Indochina Peninsula? The BB emission in this region seems far less than that in India and sub-Saharan Africa.

Responses: We have replaced Figure 2 by the one overlaid with March BC emission from BB as well as the time series of the BB emissions (BC, OC and SO₂) for both CTRL and BBER runs (Page 7 Line 137).

The sentence on Page 8 Line 162 has been modified as follows: *“The control experiment (CTRL) has the original BB emissions, while the sensitivity experiment (BBER) has the March BB emissions reduced to 15% (Fig. 2b).”*

Figure R3 shows the global distribution of annual averaged BB emission and its monthly variation from four important biomass burning regions (Ding et al., 2021). As the reviewer speculated, the total BB emission in the ICP in March–April is only about 20% of that in South Africa in June–August (Table R1). However, the cloud cover enhancement induced by the BB aerosols is similar (over 30%) in both regions, suggesting a much stronger aerosol effect on climate in the ICP (Ding et al., 2021).

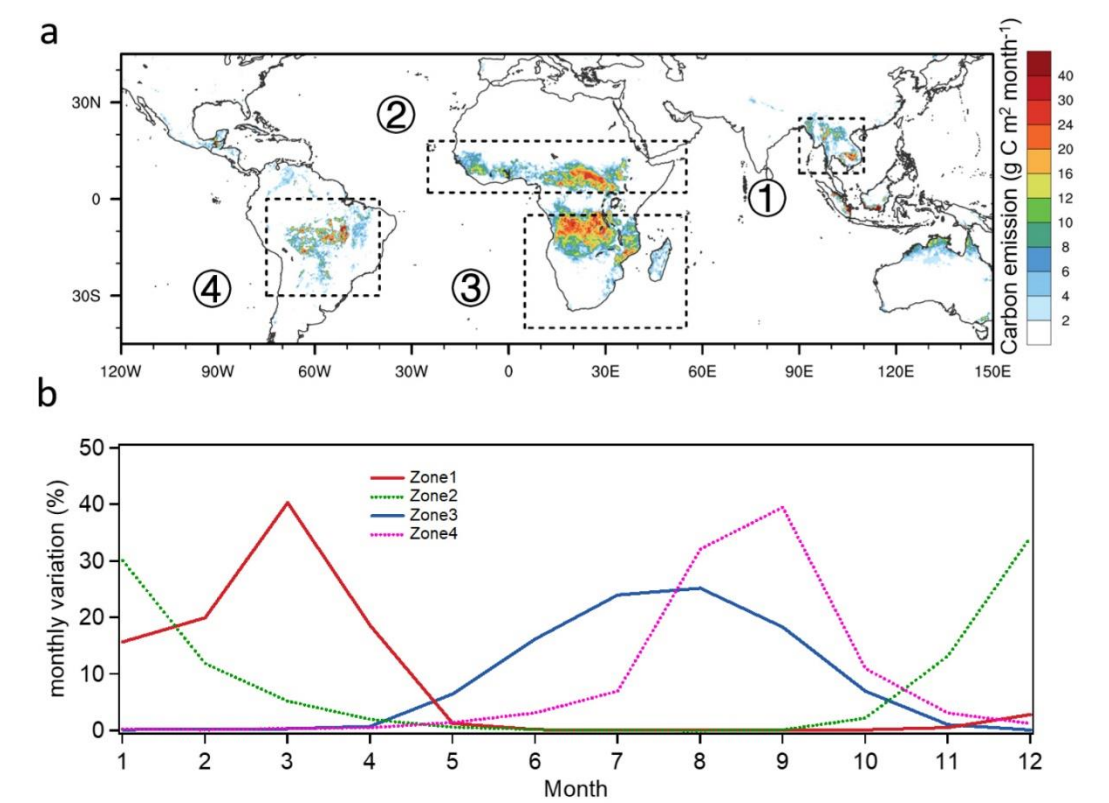


Figure R3: Biomass burning (BB) carbon emission and its seasonal patterns in main BB regions in the world. (a) Global distribution of annual averaged carbon emissions from BB. (b) Monthly variation of carbon emissions from four important BB regions: Southeast Asia, North Africa, South Africa, and the Amazon. After Ding et al. (2021).

Table R1. Averaged carbon emission in four regions with intensive BB activities during 2000-2015. After Ding et al. (2021).

Zone	Period	Total Carbon Emission (Tg C)
Zone1 –Southeast Asia	Mar–Apr.	62
Zone2 –Center Africa	Nov–Dec.	184
Zone3 –South Africa	Jul–Aug.	314
Zone4 –South America	Aug–Sep.	169

To provide a clearer picture of BB emission in the ICP region, we have added the sentence on Page 2 Line 57 as follows: “*Although the total BB emission in the ICP in March–April is only 20% of that in South Africa in June–August, the cloud cover enhancement induced by the BB aerosols is similar (over 30%) in both regions, suggesting a much stronger aerosol effect on climate in the ICP (Ding et al., 2021).*”

Although authors mentioned uncertainty in their modeling investigation, no uncertainty analysis was done. How about uncertainty in BB emissions?

Responses: To largely reduce the randomness and uncertainties introduced by initial and boundary conditions, we used ensemble simulations with six members by perturbing initial and boundary conditions and analysed the ensemble-mean results in this study. As concerned by the reviewer, we further analysed uncertainties of temperature, BC mass concentration and atmospheric heating rates (as shown in **Figure 9a**, **Figure 12c** and **Figure 14c**, respectively), and equivalent potential temperature, convective stability, and differences in convective stability (shown in **Figure 13**) in the revised manuscript.

As for the BB emissions, the uncertainty in emission inventories is mainly from a variety of measurements or analysis procedures, including detection of fire or areas burned, retrieval of fire radiative power, emission factors, biome types, burning stages, and fuel consumption estimates (Pan et al., 2020). The choice of emission inventory may markedly affect the simulated aerosols. For example, the magnitude of mean modelled smoke $\text{PM}_{2.5}$ can differ across five main inventories by $>20 \mu\text{g m}^{-3}$ in Singapore during the BB season (Liu et al., 2020b). The Quick Fire Emissions Dataset (QFED) provides a relatively large quantity of particle emissions from fires compared to the Fire INventory from NCAR (FINN) (Pan et al., 2020). While the comparison of BB emission inventories is beyond the scope of this study, the potential impact of using different inventories needs to be kept in mind. Note that the FINN version 1.5 utilized in this study is widely used in BB aerosol modelling investigations (Lee and Wang, 2020; Liu et al., 2020a; Wang et al., 2021; Takeishi and Wang, 2022). Also, our results are in agreement with many studies using other BB emission inventories. For example, the response of low cloud over subtropical Southeast Asia to March BB aerosols in this study is consistent with that of Ding et al. (2021), which used the QFED; the radiative response to BB aerosols over the ICP in this study is similar to that of Dong et al. (2019),

which used the Global Fire Emission Database v4.1; the BB aerosol-induced atmospheric circulation anomalies over the ICP agree with the results of Yang et al. (2022), which used the BB emission from the MERRA-2. It follows that although the choice of BB emission inventory may have an impact on the simulated results, it may not be sufficient to affect our qualitative conclusions.

As for the effects of BB emission reduction rate in the sensitivity experiment on our results, we have discussed them in response to the first comment. Briefly, the magnitude of the reduction rate does not influence our qualitative results, and more precise quantitative results need to be obtained by running more experiments in the future.

To consider the possible impact of BB emissions, we have added the following paragraph on Page-8 Line-152: *“Note that the choice of BB emission inventory could significantly affect the simulated aerosols due to the uncertainty in emission inventories introduced by a variety of measurements or analysis procedures, including detection of fire or areas burned, retrieval of fire radiative power, emission factors, biome types, burning stages, and fuel consumption estimates (Liu et al., 2020b; Pan et al., 2020). While the comparison of BB emission inventories is beyond the scope of this study, the FINN version 1.5 utilized in this study is widely used in BB aerosol modelling investigations (Lee and Wang, 2020; Liu et al., 2020a; Wang et al., 2021; Takeishi and Wang, 2022); nevertheless, the potential impact of using different inventories needs to be kept in mind.”*

References

- Chavan, P., Fadnavis, S., Chakroborty, T., Sioris, C. E., Griessbach, S., and Müller, R.: The outflow of Asian biomass burning carbonaceous aerosol into the upper troposphere and lower stratosphere in spring: radiative effects seen in a global model, *Atmos. Chem. Phys.*, 21, 14371-14384, 10.5194/acp-21-14371-2021, 2021.
- Ding, K., Huang, X., Ding, A., Wang, M., Su, H., Kerminen, V.-M., Petäjä T., Tan, Z., Wang, Z., Zhou, D., Sun, J., Liao, H., Wang, H., Carslaw, K., Wood, R., Zuidema, P., Rosenfeld, D., Kulmala, M., Fu, C., Pöschl, U., Cheng, Y., and Andreae, M. O.: Aerosol-boundary-layer-monsoon interactions amplify semi-direct effect of biomass smoke on low cloud formation in Southeast Asia, *Nat. Commun.*, 12, 6416, 10.1038/s41467-021-26728-4, 2021.

Dong, X., Fu, J. S., Huang, K., Zhu, Q., and Tipton, M.: Regional Climate Effects of Biomass Burning and Dust in East Asia: Evidence From Modeling and Observation, *Geophys. Res. Lett.*, 46, 11490-11499, 10.1029/2019gl083894, 2019.

Lee, D., Sud, Y. C., Oreopoulos, L., Kim, K. M., Lau, W. K., and Kang, I. S.: Modeling the influences of aerosols on pre-monsoon circulation and rainfall over Southeast Asia, *Atmos. Chem. Phys.*, 14, 6853-6866, 10.5194/acp-14-6853-2014, 2014.

Lee, H. H., and Wang, C.: The impacts of biomass burning activities on convective systems over the Maritime Continent, *Atmos. Chem. Phys.*, 20, 2533-2548, 10.5194/acp-20-2533-2020, 2020.

Liu, L., Cheng, Y., Wang, S., Wei, C., Pöhlker, M. L., Pöhlker, C., Artaxo, P., Shrivastava, M., Andreae, M. O., Pöschl, U., and Su, H.: Impact of biomass burning aerosols on radiation, clouds, and precipitation over the Amazon: relative importance of aerosol–cloud and aerosol–radiation interactions, *Atmos. Chem. Phys.*, 20, 13283-13301, 10.5194/acp-20-13283-2020, 2020a.

Liu, T., Mickley, L. J., Marlier, M. E., DeFries, R. S., Khan, M. F., Latif, M. T., and Karambelas, A.: Diagnosing spatial biases and uncertainties in global fire emissions inventories: Indonesia as regional case study, *Remote Sens. Environ.*, 237, 111557, <https://doi.org/10.1016/j.rse.2019.111557>, 2020b.

Pan, X., Ichoku, C., Chin, M., Bian, H., Darmenov, A., Colarco, P., Ellison, L., Kucsera, T., da Silva, A., Wang, J., Oda, T., and Cui, G.: Six global biomass burning emission datasets: intercomparison and application in one global aerosol model, *Atmos. Chem. Phys.*, 20, 969-994, 10.5194/acp-20-969-2020, 2020.

Takeishi, A., and Wang, C.: Radiative and microphysical responses of clouds to an anomalous increase in fire particles over the Maritime Continent in 2015, *Atmos. Chem. Phys.*, 22, 4129-4147, 10.5194/acp-22-4129-2022, 2022.

Thornhill, G. D., Ryder, C. L., Highwood, E. J., Shaffrey, L. C., and Johnson, B. T.: The effect of South American biomass burning aerosol emissions on the regional climate, *Atmos. Chem. Phys.*, 18, 5321-5342, 10.5194/acp-18-5321-2018, 2018.

Wang, J., jiang, Q., You, Y., Rao, X., Sheng, L., Gui, H., Hua, C., and Zhang, B.: Effects of Biomass Burning Aerosol in Southeast Asia on Haze and Precipitation over China, *Meteor. Mon.* (in Chinese), 47, 348-358, 2021.

Yang, S., Lau, W. K. M., Ji, Z., Dong, W., and Yang, S.: Impacts of radiative effect of pre-monsoon biomass burning aerosols on atmospheric circulation and rainfall over Southeast Asia and southern China, *Clim. Dynam.*, 10.1007/s00382-021-06135-7, 2022.

Responses to Anonymous Referee #2

This paper uses WRF-Chem model to explore the impact of biomass burning (BB) on atmospheric circulation and precipitation during the peak biomass burning season (March) in the Indochina Peninsula (ICP). Authors utilize observations to show that March BB aerosols can reduce precipitation over the ICP in March but increase precipitation from April 1-20, indicating the long-lasting effects of March BB aerosols on precipitation, but with opposite effects in the two months. However, it is hard to determine the causality between BB aerosols over the ICP and atmospheric circulation (and precipitation), just from observations. Therefore, two groups of WRF-Chem experiments: with control (CTRL) and sensitivity (BBER) model scenarios, were performed to discern the mechanisms responsible for these feedbacks of BB aerosols on precipitation. To discern the feedback effects.

The paper is very well-written with brevity and high-quality visualization of all results. The manuscript should be published once the following comments are addressed:

Responses: We greatly appreciate these comments and suggestions. The manuscript has been improved by considering these comments and suggestions. Our detail responses are given point by point below in blue. The revised text is highlighted in red.

Specific comments:

1) Section 4.1: Evaluation of model results

For comparison of CTRL AOD and Precipitation with MODIS and TRMM observations respectively, if possible, please provide some domain-wide statistical difference metrics (such as mean bias, mean error, RMSE, correlation, etc.). This will be helpful to quantify the predictive capability of the default model for the ICP region in this study period.

Responses: As suggested by the reviewer, we have evaluated statistics metrics (mean observation, mean simulation, mean bias, relative mean bias, RMSE, and pattern correlation) for AOD, precipitation and 850-hPa wind. We present them in Table S1 below (also in the supplementary):

Table S1. Evaluation Statistics for AOD, precipitation and 850-hPa wind.

Variable	Mean Obs.	Mean Sim.	Mean Bias	Relative Mean Bias (%)	RMSE	Pattern Correlation
AOD	0.44	0.33	-0.11	-25.63	0.23	0.71
Precipitation (mm day ⁻¹)	2.22	3.52	1.29	58.25	2.67	0.71
850-hPa zonal wind (m s ⁻¹)	-0.17	-0.55	-0.38	230.5	1.8	0.94
850-hPa meridional wind (m s ⁻¹)	0.44	0.30	0.14	-30.85	1.53	0.67

To present the model evaluation more quantitatively, we revised the sentence on Page 11 Line 236 as follows: “*The WRF-Chem ensemble-mean rainfall based on six CTRL members (Fig. 4b) shows a spatial pattern consistent with that in the TRMM and the pattern correlation is up to 0.71, although the model overestimates the convection in the northern tropical Indian Ocean, orographic precipitation in the northwestern ICP region, and rainfall south of Japan*”.

We have also added this sentence on Page 11 Line 238 in our revised manuscript: “*It was reported that regional climate models, including the WRF, tend to overestimate precipitation due to deficiencies within the convective cloud and microphysical schemes (Caldwell et al., 2009; Argüeso et al., 2012)*”.

The sentence on Page 12 Line 243 has been revised as follows: “*In general, the model can reasonably capture these observed circulation features with the pattern correlation of 0.94 and 0.67 for 850-hPa zonal and meridional wind components, respectively*”.

The sentence on Page 12 Line 250 has been modified as follows: “*The spatial pattern of modeled AOD is consistent with MODIS satellite retrieval, with the pattern correlation of 0.71.*”

The following sentence has been added on Page 12 Line 252: “*The model simulation underestimates the AOD by 25.63% for the whole domain.*”

We have revised the last paragraph of this section on Page 13 Line 259 as follows:

“Generally, the model reproduces well the spatial distributions of rainfall, circulation and aerosols. Specific evaluation statistics are summarized in Table S1. Given this, the ensemble-mean differences between CTRL and BBER (i.e. CTRL minus BBER) are used to examine the effects of BB aerosols and associated physical mechanisms.”

2) Besides, discerning the direct and indirect effects via sensitivity experiments with and without direct or indirect effects, doing an HYPLIT trajectory analysis to look at BB emissions trajectories in the modeling domain for the March-April period, if possible is encouraged. Trajectories of air mass relative to the black box that outlines the main Indochina Peninsula (ICP; 93°–110°E, 10°–24°N), may aid the authors’ current inferences more in explaining the opposite impacts in March vs April.

Responses: We have performed the HYPLIT model 96h (4 days) air mass trajectories forward run using the 1-degree GDAS meteorological data at four high BB emission sites (95.75°E, 18.75°N; 102°E, 18.25°N; 106.5°E, 15°N; 105.5°E, 12.5°N) representing northwestern Indochina Peninsula, northern Indochina Peninsula, mid-eastern Indochina Peninsula and southern Indochina Peninsula, respectively. The multiple iterations of the trajectory were calculated from March 1st to April 20th 2010 at every six hours. The cluster mean trajectories of air mass and their frequency analysis are showed in supplementary (Fig. S1). It is worth noting that we also only did the trajectory analysis for March, since the results were quite similar to those for March 1st–April 20th.

To better explain the cause of AOD anomaly pattern in Figure 5a, we have added the following text on Page 13 Line 265: *“The aerosol loading anomaly gradually decreased from northern ICP through the northern SCS up to the Northwest Pacific and the anomaly also declined westward from the ICP to the central Bay of Bengal (Fig. 5a). These are the results of BB aerosol dispersion downstream along with the subtropical westerlies and tropical easterlies. Lagrangian dispersion modelling for air mass shows that aerosols over the northern ICP can be transported to the northern SCS and southern China, while the aerosols over the southern ICP have westward trajectories of 11%–31% and partially reach the central Bay of Bengal (Fig. S1)”*

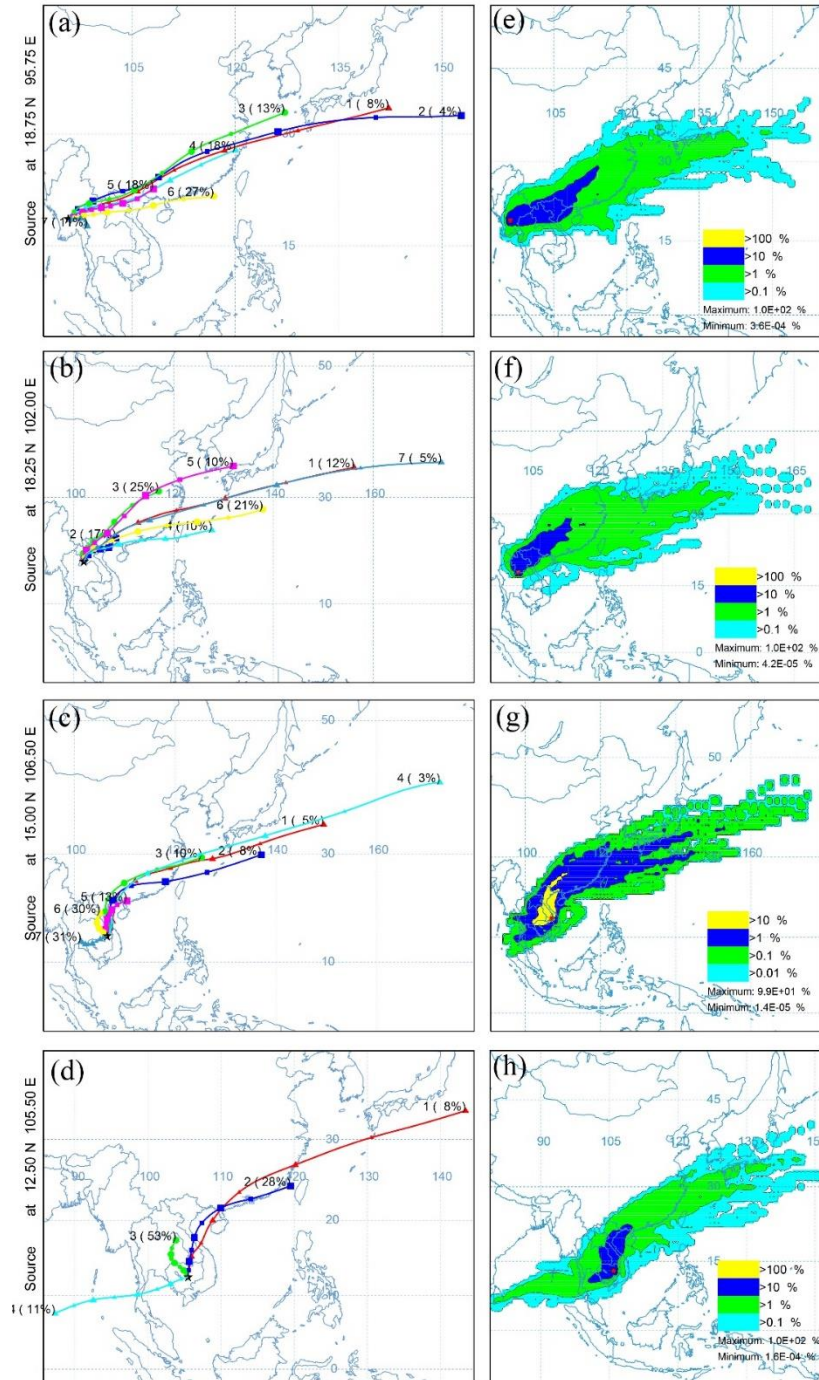


Figure S1: Distribution of cluster mean 96h (4 days) forward trajectories (a–d, left column) of air mass and their frequencies (e–h, right column) based on the Hybrid Single-Particle Lagrangian Integrated Trajectory (HYSPLIT) model for north-western Indochina Peninsula (a, e; 95.75°E, 18.75°N), northern Indochina Peninsula (b, f; 102°E, 18.25°N), mid-eastern Indochina Peninsula (c, g; 106.5°E, 15°N), and southern Indochina Peninsula (d, h; 105.5°E, 12.5°N) from March 1st to April 20th, 2010. The 1-degree meteorological data from the Global Data Assimilation System (GDAS1) was used to run the model. Note that we did the trajectory analysis only for March, since the results were quite similar to those for March 1st–April 20th.

3) Adding maybe a supplemental figure on the BB emissions for the ICP region focusing on the March-April season might be helpful in explaining the instant vs delayed impacts of BB burning aerosols in ICP regions' atmospheric circulation and precipitation patterns.

Responses: We have replaced Figure 2 by the one overlaid with March BC emission from BB and the time series of the BB emissions (BC, OC and SO₂) for both CTRL and BBER runs (Page 6 Line 137). The new Figure 2 and its caption are shown below, and the sentence around Line 162, Page 8 has been modified as follows: “*The control experiment (CTRL) has the original BB emissions, while the sensitivity experiment (BBER) has the March BB emissions reduced to 15% (Fig. 2b).*”

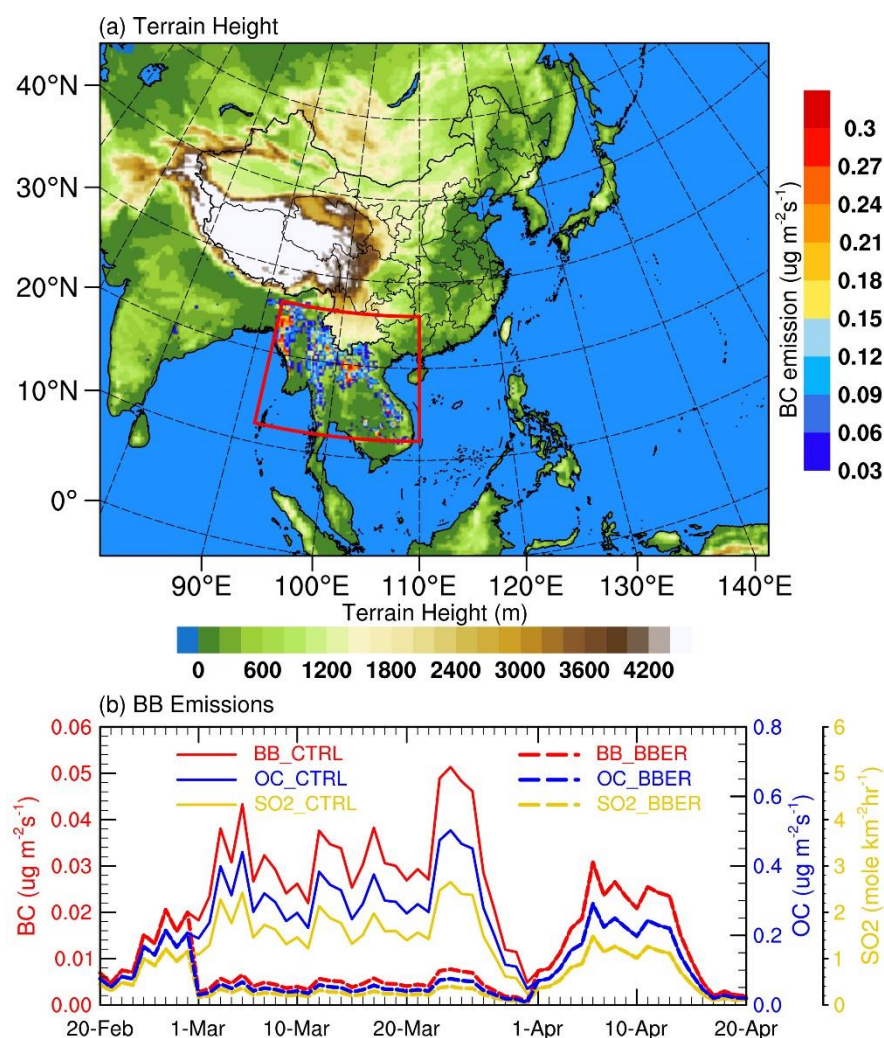


Figure 2: (a) Model domain, orography (shading; m) and March BC emission input in the model from BB based on the Fire INventory from NCAR (FINN) version 1.5. (b) The time series of BB emissions (BC, OC and SO₂) averaged over Indochina [92 °-110 °E, 12 °-26 °N; as outlined by the red box in (a)] from February

20th to April 20th 2010. The solid curves are the emissions for control experiment (CTRL). The dashed curves are the emissions for the sensitivity experiment (BBER), i.e., the March emissions are reduced to 15%.

1 Instant and delayed effects of march biomass burning aerosols over 2 the Indochina Peninsula

3 Anbao Zhu^{1,2}, Haiming Xu^{1,2}, Jiechun Deng^{1,2}, Jing Ma^{1,2}, Shaofeng Hua³

4 ¹ Key Laboratory of Meteorological Disaster/KLME/ILCEC/CIC-FEMD, Nanjing University of Information Science &
5 Technology, Nanjing 210044, China

6 ²School of Atmospheric Sciences, Nanjing University of Information Science & Technology, Nanjing 210044, China

7 ³CMA Weather Modification Centre (WMC), Beijing 100081, China

8 *Correspondence to:* Haiming Xu (hxu@nuist.edu.cn)

9 **Abstract.** Through analyzing observations and simulations from the Weather Research and Forecasting model coupled with
10 Chemistry, we investigated instant and delayed responses of large-scale atmospheric circulations and precipitation to
11 biomass burning (BB) aerosols over the Indochina Peninsula (ICP) in the peak emission of March. The results show that the
12 BB aerosols inhibit precipitation over the ICP in March, and promote precipitation from early-April to mid-April.
13 Specifically, the March BB aerosols over the ICP can induce mid-to-lower tropospheric heating and planetary boundary
14 layer cooling, to enhance local atmospheric stability; meanwhile, the perturbation heating can trigger an anomalous low in
15 the lower troposphere to moisten the mid troposphere. However, the convection suppression due to the stabilized atmosphere
16 dominates over the favorable water-vapor condition induced by large-scale circulation responses, leading to an overall
17 reduced precipitation over the ICP in March. For the delayed effect, the anomalous low can provide more water vapor as the
18 monsoon advances in early-April, although it becomes much weaker without BB aerosols' strong heating. On the other hand,
19 the convective instability above 850 hPa is enhanced by more water vapor, resulting in enhanced precipitation over the ICP,
20 northern South China Sea, and southern China. Thereafter, the condensational latent heating gradually takes over from the
21 BB aerosol radiative heating, acting as the main driver for maintaining the anomalous circulation and thus the delayed effect
22 in mid-April.

23 1 Introduction

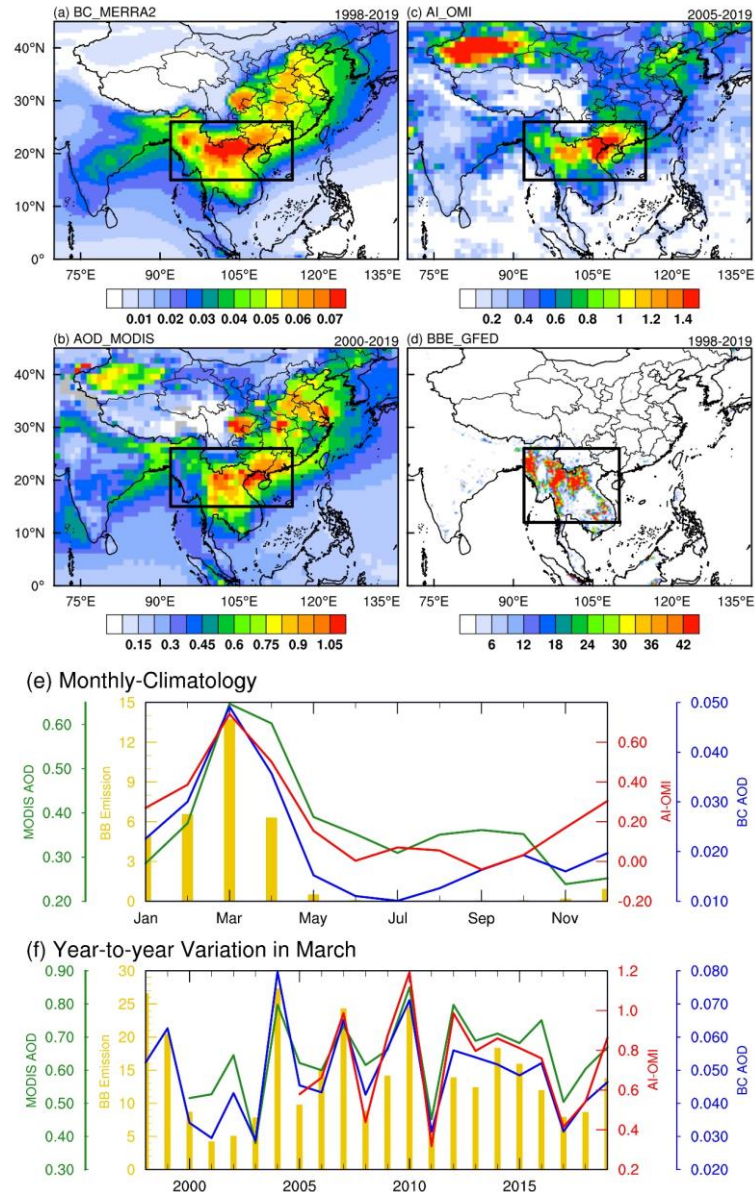
24 Biomass burning (BB), including agro-residue burning and forest or prairie fires, is one of the largest sources of many trace
25 gases and aerosol particles in the atmosphere (Reid et al., 2005). Globally, BB contributes 42% of the black carbon (BC)
26 emissions and 74% of the organic carbon (OC) emissions (Bond et al., 2004). Smoke aerosols produced by BB can reduce
27 air quality, diminish visibility and harm public health (Huang et al., 2013; Yadav et al., 2017; Requia et al., 2021). BB-
28 emitted aerosols also have vital impacts on regional climate and hydrological cycle through interactions with radiation,
29 clouds and precipitation (Koren et al., 2004; Jacobson, 2014; Hodnebrog et al., 2016; [Liu et al., 2020](#)[Liu et al., 2020a](#)). The
30 Indochina Peninsula (ICP) is one of the most active fire hotspots in the world (Lin et al., 2009; Gautam et al., 2013; Yadav et

al., 2017), with high population density, thus high social and economic relevance, and with strong monsoon circulation variability (Li et al., 2016; Wu et al., 2016). Therefore, it is essential to investigate the feedback mechanisms of BB aerosols-climate interactions to better understand aerosols' climatic and socio-economic impacts (Lau, 2016; Ding et al., 2021). BB aerosols can affect the climate in several ways. The aerosols, such as BC and OC aerosols, can directly scatter and absorb solar radiation (i.e., the so-called "direct effect"), thereby reducing the solar radiation reaching the surface. Both observational and numerical studies suggested that BB aerosols' direct effect can inhibit vertical instability by heating the atmosphere of the smoke aerosol layer and cooling the surface, thereby reducing surface fluxes and suppressing warm-cloud formation and convective activity (Koren et al., 2004; Feingold et al., 2005; Hodnebrog et al., 2016; Huang et al., 2016b), and enhancing low-cloud fraction (Sakaeda et al., 2011; Lu et al., 2018; Ding et al., 2021). On the other hand, BB aerosols can locally reduce precipitation by serving as cloud condensation nuclei and ice nuclei, increasing cloud droplet number concentration, decreasing droplet effective radii (i.e., "indirect effect"), and decelerating the autoconversion process (Lee et al., 2014; ~~Liu et al., 2020~~Liu et al., 2020a; Herbert et al., 2021). Numerical modelling studies have found that the direct effect dominates at low BB aerosol loading, while the indirect effect dominates at high BB aerosol loading (~~Liu et al., 2020~~Liu et al., 2020a; Herbert et al., 2021). However, the initial suppressive effect of BB aerosols on rainfall can lead to convective invigoration by cold rain processes (Martins et al., 2009). BB aerosols may also enhance rainfall under certain conditions, which are highly dependent on factors such as the altitude and longevity of the smoke plume (Tummon et al., 2010; Ban-Weiss et al., 2012; Herbert et al., 2021), the atmospheric degree of instability (Gonçalves et al., 2015) and the diurnal cycle of the convective system (Lee and Wang, 2020; Herbert et al., 2021). The above-mentioned perturbations caused by BB aerosols can also affect large-scale atmospheric circulation, thus changing the regional climate (Zhang et al., 2009; Lee et al., 2014; Jiang et al., 2020; Zhou et al., 2021).

The ICP experiences substantial agro-residue burning across farmlands in preparation for planting during the dry season, typically between February and April with a maximum occurrence in March (Huang et al., 2013; Shi et al., 2014) (Figs. 1a–e). Large amounts of BB aerosols are injected into the atmosphere, uplifted up to 3-km height by the India-Burma trough and transported to southern China and the South China Sea (SCS), and even to the western North Pacific Ocean by the subtropical southwesterly jet (Lin et al., 2009; Huang et al., 2013; Huang et al., 2016a; Zhu et al., 2021). The BB aerosols become minimal after the monsoon rainfall onset in late-April due to rainout and washout processes (Huang et al., 2016a). Although the total BB emission in the ICP in March–April is only 20% of that in southern South Africa in June–August, the cloud cover enhancement induced by the BB aerosols shows a similar (over 30%) in both regions, suggesting a much stronger aerosol effect on climate in the ICP (Ding et al., 2021).

The effects of BB aerosols over the ICP on regional air quality (Lin et al., 2009; Huang et al., 2013; Lin et al., 2014; Yang et al., 2022a) and climate (Lee and Kim, 2010; Lee et al., 2014; Pani et al., 2018; Dong et al., 2019; Wang et al., 2021; Yang et al., 2022b) have been widely investigated based on observations and numerical modeling studies. However, aerosol-cloud-precipitation interactions over the ICP have rarely been explored. Using an atmospheric global climate model (AGCM) coupled with an aerosol module, Lee and Kim (2010) showed that BC's radiative forcing (including anthropogenic and BB-

emitted) in East Asia induces an anomalous meridional circulation through radiation effect during spring. The anomalous upward motion near 30°N causes increased precipitation over Myanmar and Bangladesh, while the anomalous downward motion around 10°N causes a decrease in precipitation over Southeast Asia. Based on the Goddard Earth Observing System version 5 (GEOS-5)/AGCM model, Lee et al. (2014) suggested that both the direct effect (increasing lower-atmospheric stability) and indirect effect (decelerating cloud droplet autoconversion process) of BB aerosols can suppress local precipitation in the ICP during the pre-monsoon season (March–April), and the large-scale advection of cloud moisture invigorates the downwind rainfall. Yang et al. (2022b) utilized the Weather Research and Forecasting model coupled with Chemistry (WRF-Chem) to show that the increased atmospheric stability induced by BB aerosols inhibits local rainfall over the ICP. The low-level cyclonic anomaly wind induced by the BB aerosol heating can modify moisture transport, leading to increased (decreased) rainfall over the southern coast (northern inland) of southern China. A case study by Wang et al. (2021) revealed that BB aerosols transported from the ICP can suppress convective precipitation and enhance non-convective precipitation over southern China. Most of these studies focused on the seasonal time scale (Lee and Kim, 2010; Lee et al., 2014; Yang et al., 2022b) or individual cases lasting a few days (Wang et al., 2021). However, the BB emission over the ICP has a strong intra-seasonal variability peaking in March (Fig. 1e), whose instant and delayed effects on the climate remain unclear.



80

81 **Figure 1: Spatial distribution of March (a) black carbon (BC) aerosol optical depth (AOD; shading, unitless) averaged over 1998–**
 82 **2019 from MERRA-2, (b) AOD (unitless) averaged over 2000–2019 from MODIS Terra, (c) aerosol index (AI; unitless) averaged**
 83 **over 2005–2019 from OMI, and (d) biomass burning (BB) carbon emission (shading; $\text{g C m}^{-2} \text{ month}^{-1}$) averaged over 1998–2019**
 84 **from GFEDv4.1. (e) Monthly climatology of BB aerosol indices (blue line for BC AOD, green line for AOD, red line for AI) and**
 85 **emission (gold bar) averaged over Indochina [92°–115°E, 15°–26°N for BC AOD, AOD and AI; 92°–110°E, 12°–26°N for BB**
 86 **emission; as outlined by the black boxes in (a–d)]. (f) Same as (e), but for the time series of monthly averaged BB aerosol indices in**
 87 **March.**

88 In this study, we examine the impacts of March BB aerosols over the ICP using both observations and model experiments. In
 89 particular, we address the following questions: (1) What are the instant and delayed effects of March BB aerosols over the
 90 ICP on atmospheric circulation and precipitation? (2) What are the differences between these two effects and what are their

underlying physical mechanisms? The remaining paper is organized as follows. In Sect. 2, we describe the data, methods, model, and experimental design. In Sect. 3, we present the observed evidence of BB aerosol impacts on circulation and precipitation. In Sect. 4, we discuss the responsible physical mechanisms based on simulation results. Conclusions and discussion are provided in Sect. 5.

2 Methodology

2.1 Data and statistical methods

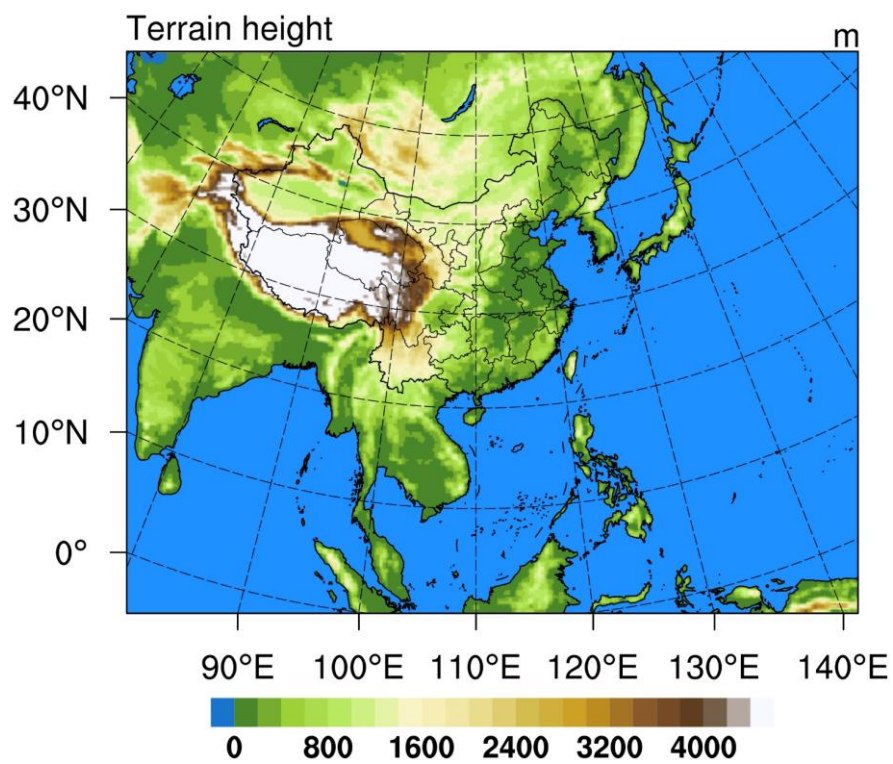
The meteorological and BC aerosol data used in this study are the Modern Era Retrospective analysis for Research and Applications Version 2 (MERRA-2) from the National Aeronautics and Space Administration (NASA) Global Modeling and Assimilation Office (GMAO) (Gelaro et al., 2017), with a spatial resolution of 0.5° by 0.65° (longitude by latitude) on 72 levels. MERRA-2 reanalysis is the first satellite era (1980 onward) reanalysis data jointly assimilating meteorological and aerosol observations. The MERRA-2 aerosol data is produced using the Goddard Chemistry Aerosol Radiation and Transport (GOCART) aerosol model coupled to the GEOS-5 data assimilation system. The GOCART model simulates five aerosol species: dust, black carbon, organic carbon, sulfate and sea salt. The GEOS-5 assimilates the bias-corrected aerosol optical depth (AOD) from the Advanced Very High Resolution Radiometer (AVHRR) instrument over the ocean (Heidinger et al., 2014), the Moderate resolution Imaging Spectroradiometer (MODIS) from the Terra and Aqua satellites (Levy et al., 2010), Multiangle Imaging SpectroRadiometer (MISR) AOD over land (Kahn et al., 2005), and ground-based Aerosol Robotic Network (AERONET) AOD (Holben et al., 1998). Numerous evaluations on the MERRA-2 aerosol data have shown that both the AOD and the vertical structure of aerosol properties in the MERRA-2 have good agreement with the observations (Buchard et al., 2017). In this study, we use the monthly mean BC AOD.

We also use the AOD from 1° MODIS Terra Level-3 monthly product (MOD08_M3) (Gupta et al., 2016), aerosol index (AI) from 1° Ozone Monitoring Instrument (OMI)/Aura Level-3 daily product (OMAERUVd) (Torres et al., 2007) and BB emissions from the Global Fire Emissions Database version 4.1 (GFEDv4) (Randerson et al., 2017) to compare with MERRA-2 BC AOD. In addition, we use the atmospheric fields from the fifth generation European Centre for Medium-Range Weather Forecasts (ECMWF) reanalysis data (ERA5) (Hersbach and Dee, 2016), including zonal and meridional wind components on 0.25° grid. The monthly and daily precipitation data on 0.25° grid is from the Tropical Rainfall Measuring Mission (TRMM) Multi-satellite Precipitation Analysis (TMPA) 3B43 and 3B42 (Huffman et al., 2007), respectively.

For consistency, the precipitation data from the TRMM, the ERA5 reanalysis data, the GFEDv4 BB emissions, and MERRA-2 BC AOD all cover the same period of 1998–2019. MODIS AOD and OMI AI cover the periods of 2000–2019 and 2005–2019, respectively. In this study, we focus on the effect of March BB aerosols on regional climate in early-spring (March 1st–April 20th), including the instant effect in March and the delayed effect in early-April (1st–10th) and mid-April (11th–20th). The linear-regression analysis is used and subjected to the two-tailed Student's *t*-test for statistical significance.

123 **2.1 Model and experimental design**

124 In this study, the WRF-Chem version 4.2.1 is used to simulate the evolution of BB aerosols and trace gases, to investigate
125 their interactions with meteorological conditions over the ICP and East Asia. The model is configured to cover the Bay of
126 Bengal, ICP and East Asia (Fig. 2) with 331×255 grids at 27-km horizontal resolution and 42 levels from the ground to 50
127 hPa. The planetary boundary layer (PBL) processes are parameterized using the Mellor-Yamada-Janjic (MYJ) scheme with
128 local vertical mixing (Janjić, 1994), combined with the Noah Land Surface Model and the Monin-Obukhov scheme for the
129 surface layer physical processes and the interaction with land surface (Chen et al., 2010; Pahlow et al., 2001). The Rapid
130 Radiative Transfer Model for General circulation models (RRTMG) coupled with aerosol radiative effect is used for both
131 shortwave (SW) and longwave (LW) radiation (Iacono et al., 2008). The double-moment Morrison microphysics scheme
132 (Morrison et al., 2009) and Grell-Freitas (GF) cumulus scheme (Grell and Freitas, 2014) are used to ensure that aerosol
133 indirect effects are included. The Carbon-Bond Mechanism version Z (CBMZ) gas-phase chemistry mechanism combined
134 with the Model for Simulating Aerosol Interactions and Chemistry (MOSAIC) aerosol module (Zaveri and Peters, 1999;
135 Zaveri et al., 2008) are selected for aerosol simulation. Aerosol optical properties are calculated based on the Maxwell
136 approximation (Bohren and Huffman, 1983).



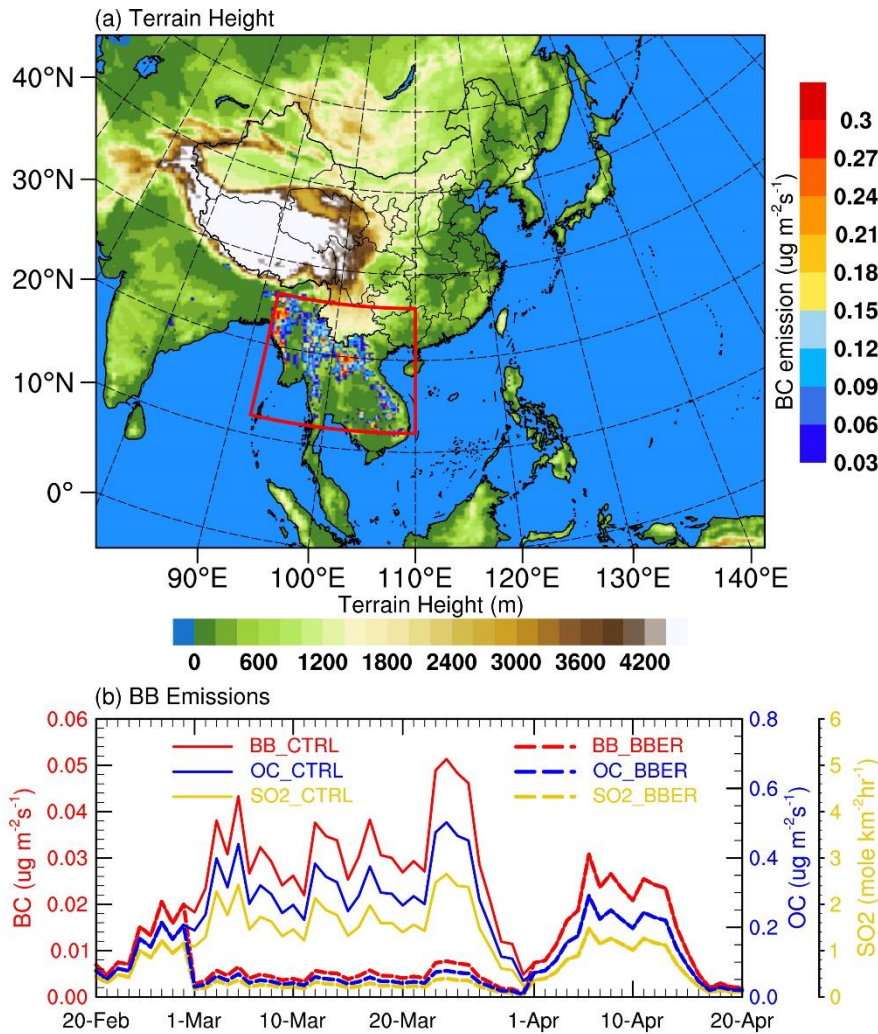


Figure 2: (a) Model domain, and orography (shading; m) and March BC emission input in the model from BB based on the Fire INventory from NCAR (FINN) version 1.5. (b) The time series of BB emissions (BC, OC and SO₂) averaged over Indochina [92 °–110 °E, 12 °–26 °N; as outlined by the red box in (a)] from February 20th to April 20th 2010. The solid curves are the emissions for control experiment (CTRL). The dashed curves are the emissions for the sensitivity experiment (BBER), i.e., the March emissions are reduced to 15%.

The boundary and initial conditions of meteorological fields are derived from the National Centers for Environmental Prediction (NCEP) Final Analysis (FNL) data with 1 ° spatial resolution and 6-h temporal interval. The input sea-surface temperature (SST) data is the NCEP real time global SST analysis. The anthropogenic emission source comes from the Multi-resolution Emission Inventory for China (MEIC) database for China (Li et al., 2017a) and from the MIX inventory (Li et al., 2017b) for regions outside of China. The biogenic emissions are calculated online using the Model of Emissions of Gases and Aerosols from Nature (MEGAN) (Guenther et al., 2012). The GOCART dust emission scheme with the Air Force Weather Agency (AFWA) modifications (LeGrand et al., 2019) is used to simulate dust emissions. The high-resolution fire

emissions based on the Fire INventory from NCAR (FINN) version 1.5 (Wiedinmyer et al., 2011) are selected as the BB emissions. Specific settings are listed in Table 1.

Note that the choice of BB emission inventory could significantly affect the simulated aerosols due to the uncertainty in emission inventories introduced by a variety of measurements or analysis procedures, including detection of fire or areas burned, retrieval of fire radiative power, emission factors, biome types, burning stages, and fuel consumption estimates (Liu et al., 2020b; Pan et al., 2020). While the comparison of BB emission inventories is beyond the scope of this study, the FINN version 1.5 utilized in this study is widely used in BB aerosol modelling investigations (Lee and Wang, 2020; Liu et al., 2020a; Wang et al., 2021; Takeishi and Wang, 2022); nevertheless, the potential impact of using different inventories needs to be kept in mind.

Table 1. WRF-Chem model parameterization option settings and emissions used in this study

Option name	Scheme
Longwave radiation	RRTMG
Shortwave radiation	RRTMG
Microphysics	Morrison 2-mom
Boundary layer	MYJ
Cumulus	Grell-Freitas
Land surface	Unified Noah
Surface layer	MM5 Monin-Obukhov
Aerosol chemistry	MOSAIC
Gas chemistry	CBMZ
Photolysis	Fast-J
Aerosol mixing rule	Maxwell–Garnett approximation
Dust emissions	GOCART-AFWA
Biogenic emissions	MEGAN version 2
Anthropogenic emissions	MEIC for China and MIX for outside of China
Biomass burning emissions	FINN version 1.5

To investigate the impacts of March BB aerosols on radiation, circulation and precipitation, we conduct two groups of simulations with different BB emission scenarios and compare these results. The control experiment (CTRL) has the original BB emissions, while the sensitivity experiment (BBER) has the March BB emissions reduced to 15% (Fig. 2b). To increase the robustness of our findings, we use six ensemble members for each experiment by perturbing initial and boundary conditions, that is, the ensemble simulations start at one day apart on February 20th–25th, 2010, respectively, and all end on

167 April 30th, 2010. Thus, different starting day in February for each member is discarded as spin-up time, and we only focus on
 168 the period from March 1st to April 20th, 2010. We chose the year of 2010 for modeling because the BB emission in 2010 was
 169 ~~above the average and greater than its climatology by about 1.7 standard deviations. We reduced BB emission to 15% in as~~
 170 ~~the sensitivity experiment in this study, because the March BB emission over the ICP in 2001, the year with the lowest BB~~
 171 ~~emission during 1998–2019, is roughly 15% of that in 2010. It would be more realistic was about six times higher than that in~~
 172 ~~2001 (the lowest year during 1998–2019 and similar to the BB reduction used in BBER; Fig. 1f), which is suitable for~~
 173 ~~investigating_ to investigate~~ the effects of BB aerosols on atmospheric circulation and precipitation on the interannual
 174 timescale.

175 3 Observations

176 3.1 Variation in BB aerosols

177 For observational evidence of possible responses of atmospheric circulation and precipitation to BB aerosols, we first
 178 examine the spatial distribution of the climatological mean BB aerosols in March (Figs. 1a–d) and their temporal variation
 179 (Fig. 1f) via multiple data sources. The spatial pattern of BB aerosols from the aerosol reanalysis data (MERRA-2) is quite
 180 consistent with multiple satellite retrievals (Figs. 1a–d). The high BC aerosol loading is concentrated in the northern ICP
 181 with a maximum BC AOD exceeding 0.07 (Fig. 1a), which is contributed by BB emissions (Fig. 1d). High BC AOD also
 182 appears over the Sichuan Basin and central-eastern China, likely caused by anthropogenic activities (Qin and Xie, 2012;
 183 Ning et al., 2018). High MODIS AOD values are also seen over northwestern China (Fig. 1b), as large dust aerosols are
 184 emitted from the Taklimakan Desert in March (Bao et al., 2009). As positive AI generally represents absorbing aerosols
 185 (dust and smoke), high AI is found over the northern ICP and northwestern China (Fig. 1c). Unlike the high BC loading over
 186 the Sichuan Basin and central-eastern China (Fig. 1a), the AI is small over these regions likely because the AI's sensitivity to
 187 aerosol amount increase more or less proportionally with the aerosol layer height, while any aerosol below about 1000 m is
 188 unlikely to be detected (de Graaf et al., 2005). The dust and BB aerosols are transported eastward at higher atmospheric
 189 levels and are more easily detected, whereas anthropogenic pollution transport mainly occurs within the boundary layer,
 190 giving rise to smaller AI (Kaskaoutis et al., 2010).

191 For temporal variation, the BC AOD from the MERRA-2 over the ICP agrees well with satellite datasets and BB emissions.
 192 Figure 1f shows the time series of area-averaged monthly BB aerosol indices in March for the northern ICP (92 °–115 °E, 15 °–
 193 26 °N for BC AOD, AOD and AI; 92 °–110 °E, 12 °–26 °N for BB emissions). The correlations between the time series of
 194 MERRA-2 BC AOD and MODIS AOD (2000–2019), AI (2005–2019), and BB emission (1998–2019) are 0.90, 0.93 and
 195 0.85, respectively; all are statistically significant at the 99 % level. This indicates that the BB aerosols over the ICP have
 196 large interannual fluctuation in March, consistent with the recent study by Ding et al. (2021) based on multiple satellite
 197 records. However, such interannual variation could be influenced by meteorological factors such as the India-Burma trough
 198 (Huang et al., 2016a) and El Niño–Southern Oscillation (ENSO) (Zhu et al., 2021). On the other hand, the interannual

199 fluctuation can be used to detect climate effects of the aerosols. Given this, we define a BB aerosol index (BBAI) the time
200 series of MERRA-2 BC AOD (1998–2019, blue line in Fig. 1f) to explore BB aerosols’ effects on atmospheric circulation
201 and precipitation.

202 **3.2 Relationship between BB aerosols and precipitation**

203 Figure 3 shows the regressed anomalies of BC AOD, precipitation and 850-hPa wind upon the BBAI in March and in early-
204 to-mid April. In March, significant positive BC AOD anomalies are seen over the ICP, northern SCS, southern China, and
205 the ocean south of Japan (Fig. 3a), as the BB aerosols emitted from the central and northern ICP are transported eastward by
206 the prevailing winds (Lin et al., 2009; Huang et al., 2013; Huang et al., 2016a; Huang et al., 2020). Correspondingly, the
207 rainfall over the ICP is reduced by anomalous westerly wind, while the rainfall in coastal Southeast China is enhanced by
208 anomalous southerly wind (Fig. 3d), forming a dipole anomaly structure.

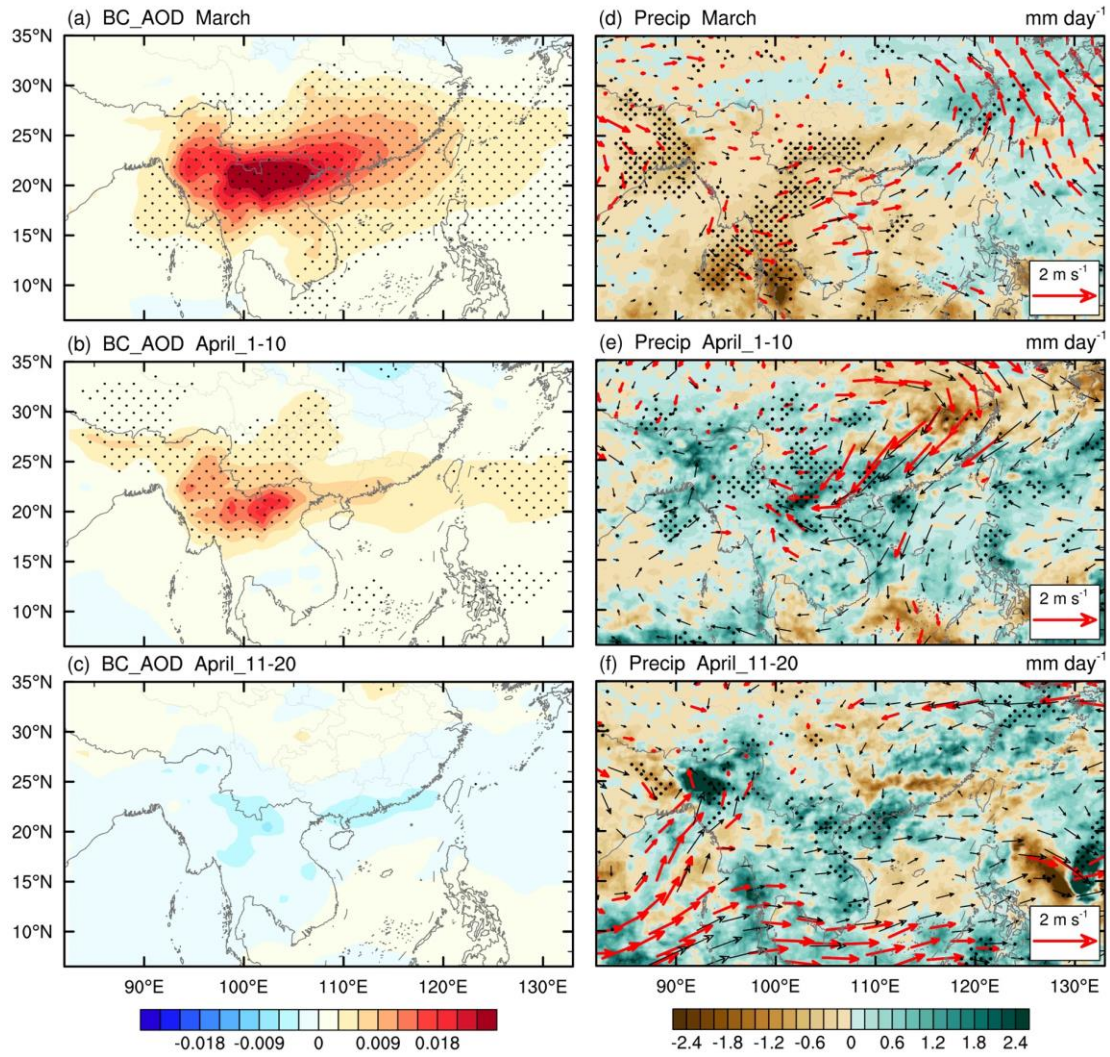


Figure 3: Regressions of anomalies in (a–c) BC AOD (shading; unitless) and in (d–f) precipitation (shading; mm day⁻¹) and 850-hPa wind (vector; m s⁻¹) onto standardized BBAI in (a, d) March, and in (b, e) early-April and (c, f) mid-April. Stippling (red vector) denotes the regressed anomalies of BC AOD and precipitation (of wind) are statistically significant at the 95% confidence level based on Student's *t*-test.

Generally, the lifetime of BB aerosols and their eastward transport life cycle last a few days to weeks (Deng et al., 2008; Huang et al., 2020; Adam et al., 2021). Thus, significant positive BC AOD anomalies are still observed over the northern ICP, southwestern China and the Northwest Pacific east of Taiwan in early-April (Fig. 3b). However, the precipitation anomaly pattern is roughly opposite to that in March, with above-normal precipitation from the northern Bay of Bengal eastward to the northern SCS and below-normal precipitation over the middle and lower reaches of the Yangtze River (Fig. 3e). Correspondingly, significant anomalous northeasterly wind occurs from the middle and lower reaches of the Yangtze River toward the northern ICP, acting to reduce the climatological south-westerly wind and the water-vapor transport in southern China. When mid-April comes, no significant BB aerosol anomalies can be found (Fig. 3c), but the positive

precipitation anomalies still exist over the northern and eastern ICP and the Beibu Gulf, accompanied by anomalous westerly wind across the Indo-Pacific Ocean and southwesterly wind from the northern tropical Indian Ocean to the northwestern ICP (Fig. 3f). As no significant anomalies are found in circulation and precipitation after about April 20th, we will focus on the features in early- to mid-April.

As mentioned above, the March BB aerosols can reduce precipitation over the ICP in March but increase precipitation from April 1st to around April 20th, indicating that the effects of March BB aerosols on precipitation can last from March to early- to-mid April, but with opposite effects in the two months. Due to the covariation of aerosols and meteorological fields, it is hard to determine the causality between BB aerosols over the ICP and atmospheric circulation (and precipitation), especially using instant observations. Therefore, in the following section, we will use two groups of WRF-Chem experiments to reveal the physical mechanisms responsible for these relationships.

4 Numerical modeling results

4.1 Evaluation of model results

Figures 4a–b illustrate the spatial patterns of the observed and modelled rainfall and 850-hPa wind averaged from March 1st to April 20th, 2010. The TRMM data shows a large rainfall belt extending from the Nanling Mountains to the south of the Yangtze River (110°–120°E, 23°–30°N) (Fig. 4a), known as spring persistent rainfall in Jiangnan of China (SPRJ). (Note: Jiangnan is the name in Chinese for the region south of the Yangtze River). In addition, large amounts of precipitation can also be found over the northwestern ICP region, which is typical orographic precipitation on the windward side of the slope. The WRF-Chem ensemble-mean rainfall based on six CTRL members (Fig. 4b) shows a spatial pattern consistent with that in the TRMM and the pattern correlation is up to 0.71, although the model overestimates the convection in the northern tropical Indian Ocean, orographic precipitation in the northwestern ICP region, and rainfall south of Japan. Similar overestimate tropical convection and orographic precipitation can be seen in Yang et al. (2022b) using the same model. It was reported that regional climate models, including the WRF, tend to overestimate precipitation due to deficiencies within the convective cloud and microphysical schemes (Caldwell et al., 2009; Argüeso et al., 2012). The atmospheric circulation in East Asia during early-spring (March 1st–April 20th) 2010 is featured by strong easterly winds across the tropical Indo-Pacific Ocean and southwesterly winds from the Bay of Bengal and SCS to southern China (Fig. 4a). In general, the model can reasonably capture these observed ~~features of rainfall and~~ features with the pattern correlations of 0.94 and 0.67 for the 850-hPa zonal and meridional wind components, respectively.

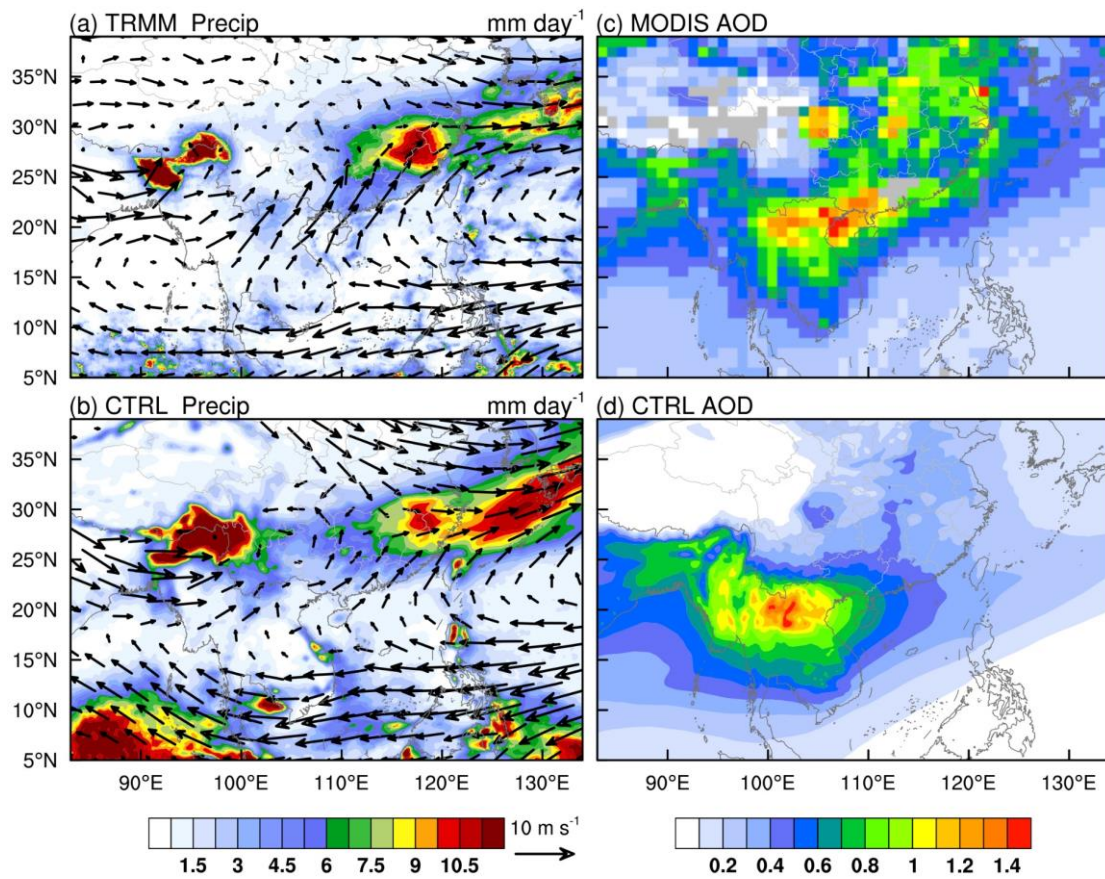


Figure 4: Spatial distributions of precipitation (shading; mm day⁻¹) and 850-hPa wind (vector; m s⁻¹) averaged over early spring (March 1st to April 20th) of 2010 from (a) observations (TRMM precipitation and ERA-5 wind) and (b) ensemble-mean of WRF-Chem CTRL. (c, d) Same as (a, b), but for AOD (shading; unitless) from (c) MODIS and (d) ensemble-mean of WRF-Chem CTRL.

The spatial pattern of modeled AOD is consistent with MODIS satellite retrieval, with the pattern correlation of 0.71. Figures 4c–d show that the WRF-Chem can capture the observed high aerosol loading over the ICP; however, it underestimates the AOD over eastern China and its coastal regions. The model simulation underestimates the AOD by 25.63% for the whole domain.–The differences between model simulations and satellite data could be attributed to two potential factors. First, the WRF-Chem model does not fully cover the effect of relative humidity on AOD calculation, as increased relative humidity can lead to higher AOD because of aerosol humidification (Myhre et al., 2007). Second, the GOCART AFWA scheme can underestimate the dust aerosol concentration in northwestern China (Zhao et al., 2020), resulting in a lower AOD in northern China. Nevertheless, the WRF-Chem model has a good performance in simulating the BB aerosols over the ICP.

Generally, the model reproduces well the spatial distributions of rainfall, circulation and aerosols. Specific evaluation statistics are summarized in Table S1. Given this, the ensemble-mean differences between CTRL and BBER (i.e. CTRL minus BBER) are used to examine the effects of BB aerosols and associated physical mechanisms.

266 4.2 Effects of BB aerosols

267 Figure 5 shows the BB aerosol-induced differences in AOD, rainfall and 850-hPa wind during March and early-to-mid April
268 of 2010. The BB aerosols significantly increased in March due to BB emissions, with a maximum AOD anomaly exceeding
269 1.2 over the northern ICP (Fig. 5a). The aerosol loading anomaly gradually decreased from northern ICP through the
270 northern SCS up to the Northwest Pacific and the anomaly also declined westward from the ICP to the central Bay of Bengal
271 (Fig. 5a). These are the results of BB aerosol dispersion downstream along with the subtropical westerlies and tropical
272 easterlies. Lagrangian dispersion modelling for air mass shows that aerosols over the northern ICP can be transported to the
273 northern SCS and southern China, while the aerosols over the southern ICP have westward trajectories of 11%–31% and
274 partially reach the central Bay of Bengal (Fig. S1). The AOD anomaly pattern of AOD agrees well with observations (Fig.
275 3a). The BB aerosol-induced anomalous circulation exhibits a belt-shaped low-pressure band in the lower troposphere (850
276 hPa) over Southeast Asia, with two centers located to the east (Hainan Island) and west (coastal southern Myanmar) of the
277 ICP (Fig. 5d). Correspondingly, the precipitation decreased by roughly 13% from the northern Bay of Bengal to southern
278 China. This was probably because the anomalous easterly wind on the northern flank of the low-pressure zone acted to
279 weaken the prevailing southwesterly wind (Fig. 4b), thereby reducing the moisture transport from the Bay of Bengal and
280 SCS. In addition, the precipitation was reduced by about 15% over most of the ICP (Fig. 5d), which was the emission source
281 region. This might be related to the suppressive effect of BB aerosols on local convection (Hodnebrog et al., 2016; Yang et
282 al., 2022b). The largest rainfall reduction occurred in the northwestern ICP, with a maximum exceeding 2 mm day⁻¹. The BB
283 aerosol-induced rainfall reduction over the emission source region is consistent with observations (Fig. 3d). Enhanced
284 precipitation occurred in the western and northern SCS, East China Sea, and their coastal regions, under southerly wind
285 anomalies. These simulated changes in rainfall and circulation induced by March BB aerosols agree well with the results
286 based on climate models (Lee et al., 2014; Chavan et al., 2021) and mesoscale weather models (Wang et al., 2021; Yang et
287 al., 2022b).

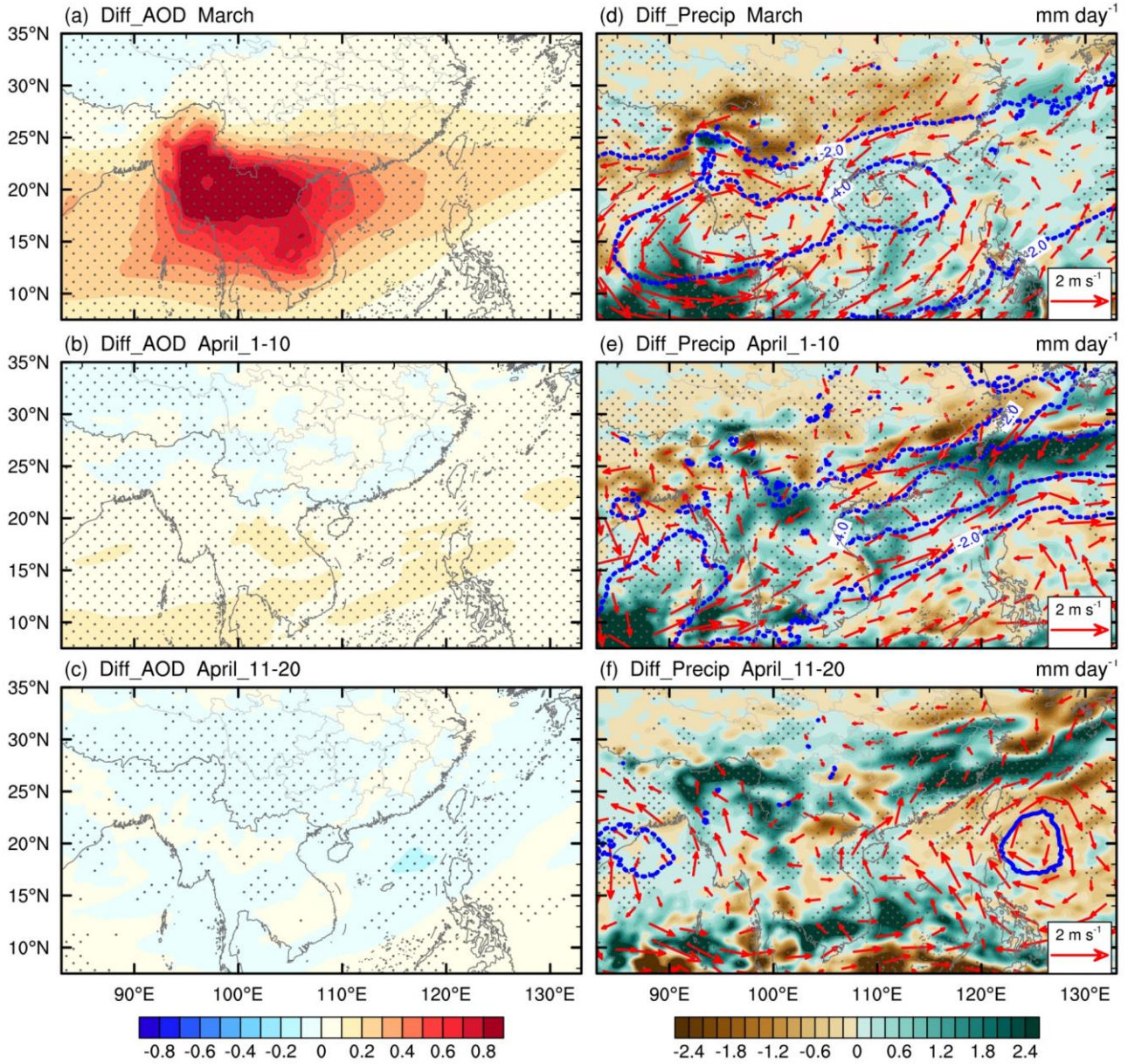


Figure 5: WRF-Chem-simulated ensemble-mean differences in (a–c) AOD (shading; unitless) and (d–f) precipitation (shading; mm day⁻¹), 850-hPa wind (vector; m s⁻¹) and geopotential height (blue contours with interval of 2 dagpm; the dashed contours are for negative values and the zero contour is omitted for clarity) between CTRL and BBER (i.e., CTRL minus BBER) during (a, d) March, (b, e) early-April and (c, f) mid-April of 2010. Stippling (red vector) denotes the AOD and precipitation (wind) are statistically significant at the 95% confidence level based on Student's *t*-test.

As in the observations (Fig. 3b), positive aerosols anomalies due to March BB emissions were still evident (albeit smaller) in early-April (Fig. 5b). The centers of the belt-shaped anomalous low at 850 hPa were located over coastal southern China and the southern Bay of Bengal (Fig. 5e). This indicates that the circulation response to March BB aerosols did not disappear immediately and could last from March to early-April, although it became weak. However, the precipitation promotion due

298 to March BB aerosols dominated over the entire ICP region in early-April, contrary to the rainfall reduction in March.
 299 Besides, the SPRJ rainband shifted markedly southward characterized by reduced precipitation in the middle and lower
 300 reaches of the Yangtze River and by increased precipitation from coastal Southeast China to the East China Sea. These
 301 responses of rainfall and circulation to March BB emissions are similar to those in observations shown in Sect. 3.2. Since
 302 aerosol concentration anomalies in April were affected a little by the March BB emissions, the anomalous rainfall in early-
 303 April could be potentially caused by the large-scale circulation change.
 304 During mid-April, no significant AOD differences appeared over the ICP (Fig. 5c). The BB aerosol-induced belt-shaped
 305 850-hPa low-pressure band almost dissipated, with only small cyclonic anomaly wind in the northern Bay of Bengal (Fig. 5f).
 306 The anomalous southerly wind in the western ICP transported moisture from the Bay of Bengal to the northern ICP and
 307 increased precipitation in the northwestern IPC along the topography on the southeastern side of the Tibetan Plateau. Clearly,
 308 the observed circulation and precipitation anomalies in mid-April (Fig. 3f) can also be reproduced in the WRF-Chem model.

309 **4.3 Physical mechanism underlying the BB aerosols-rainfall relationship**

310 **4.3.1 Instant effect**

311 The BB aerosols can significantly change radiative forcing by absorption and scattering of solar radiation, leading to spatial
 312 perturbation and redistribution of energy (Chavan et al., 2021). Figures 6a–c show the BB aerosol-induced changes in net
 313 downward SW radiative fluxes at the top of the atmosphere (TOA), in the atmosphere, and at the surface under all-sky
 314 conditions in March. BB aerosols can absorb SW radiation and heat up the atmosphere. Thus, positive SW radiation
 315 anomalies dominate in the atmosphere over the regions with high BB aerosol loading, with a magnitude of 30–65 W m⁻²
 316 from the Bay of Bengal across the ICP to the coastal region of South China and the SCS (Fig. 6b). At the surface, BB
 317 aerosols prevent the solar radiation from reaching the surface by scattering and absorption, which causes a surface cooling
 318 effect over the high BB aerosol loading regions, as shown in Fig. 6c. The maximum magnitude of the negative SW radiative
 319 flux anomalies is about 60 W m⁻² in the northern ICP. The above BB aerosol-induced SW radiative forcing both in the
 320 atmosphere and at the surface are comparable in magnitudes to those found previously (Lin et al., 2014; Pani et al., 2018;
 321 Yang et al., 2022b).

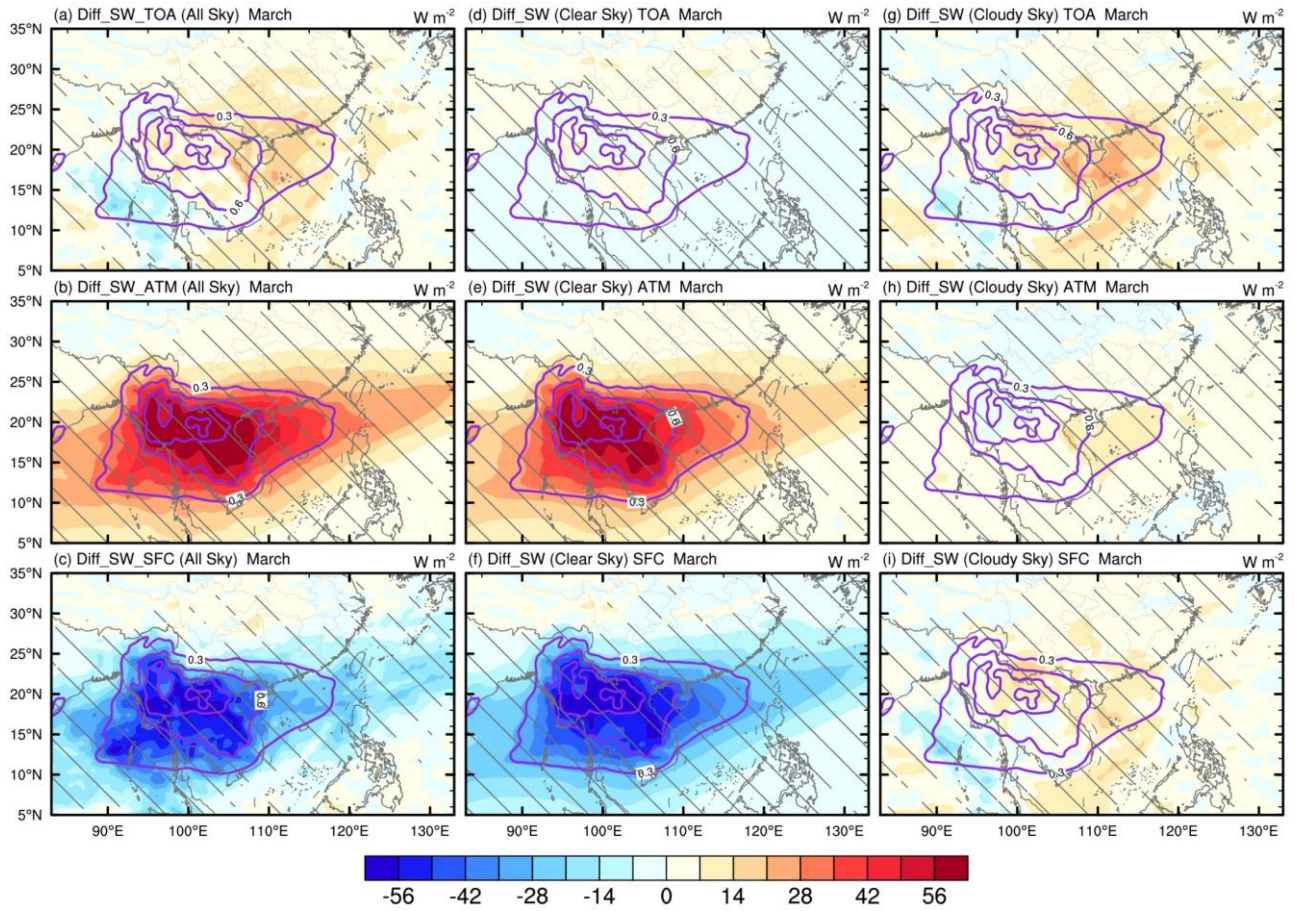
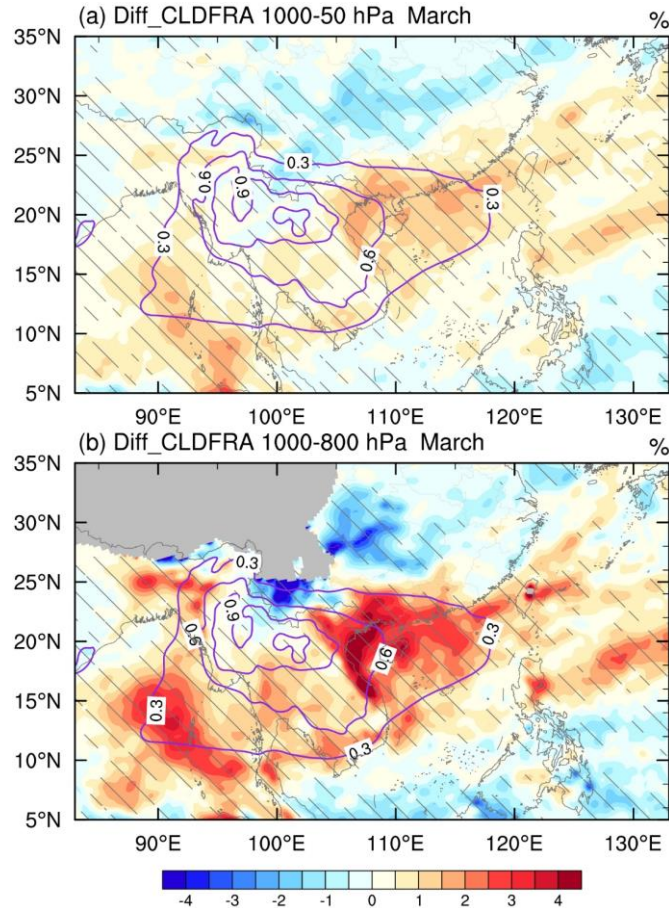


Figure 6: (a–c) Differences (CTRL minus BBER) in all-sky net downward shortwave radiative flux (shading; W m^{-2}) (a) at the top of atmosphere (TOA), (b) in the atmosphere (ATM), and (c) at the surface (SFC) in March 2010. (d–f) and (g–i) Same as (a–c), but for clear-sky and cloudy-sky differences, respectively. The purple contours with interval of 0.3 denote AOD differences (CTRL minus BBER). Hatching denotes the radiative effect is statistically significant at the 95 % confidence level based on Student's *t*-test.

At the TOA, the positive all-sky SW radiative flux anomalies induced by BB aerosols are above 15 W m^{-2} over North Vietnam, southern China and the SCS but below 7.5 W m^{-2} over the BB emission source region in the northern ICP (Fig. 6a), which is consistent with previous results in both modeling (Lee and Kim, 2010; Dong et al., 2019) and measurement studies (Pani et al., 2016; Pani et al., 2018). Generally, BB aerosols can reflect and scatter more SW radiation back to space compared to BB aerosol-free cases, leading to a weak negative SW radiative forcing at the TOA, as demonstrated in some studies (Lee et al., 2014; Lin et al., 2014; Chavan et al., 2021; Yang et al., 2022b). Nevertheless, absorbing BB aerosols can also switch from exerting a negative to a positive SW radiative effect at the TOA, due to increased underlying cloud coverage or brightness of the underlying layer (Chand et al., 2009; Lu et al., 2018). Thus, in clear-sky conditions (i.e., radiative forcing by aerosols without the cloud-circulation feedback), the TOA SW radiative effect is negative over waters and weak positive over most of the land (Fig. 6d) due to the high surface albedo contrast between those two underlying surfaces, while the strong TOA positive radiative effect over the downstream regions of the BB aerosols' transport is mainly

338 due to the cloud-circulation feedback. Figures 6g–i show the radiative effects caused by changes in cloud fraction (measured
 339 as the all-sky minus clear-sky radiative effects). Positive radiative effects in cloudy conditions are mostly distributed along
 340 the coastal regions and the ocean waters off southern China and North Vietnam, with a magnitude of 14–28 W m⁻². Greater
 341 cloud covers occur in these regions (Fig. 7a), which are concentrated in the lower troposphere (i.e., 1000–800 hPa; Fig. 7b).
 342 A previous study demonstrated that the enhancement of low clouds beneath the BB aerosol plume around 3 km over
 343 subtropical East Asia is caused by a synergetic effect of aerosol-cloud-boundary layer interaction with the monsoon (Ding et
 344 al., 2021). In turn, the BB aerosol plume uplifted above the clouds could absorb more solar radiation reflected from the cloud
 345 top, thus reducing the shortwave radiation reflected back to space (Dong et al., 2019). This also means that the increasingly
 346 thick and bright cloud layer underneath the BB aerosol plume would further amplify the direct warming effect in the
 347 atmosphere induced by BB aerosols (Ding et al., 2021), resulting in an increase of atmospheric warming by roughly 15%–20%
 348 (Fig. 6h). The spatial pattern of the net (LW+SW) radiative effect is dominated by the SW radiative effect, because the LW
 349 radiative effect is relatively small. Thus, the LW and net radiative effects are not shown here.



350 **Figure 7: Differences (CTRL minus BBER) in cloud fraction (shading; %) in the (a) entire atmospheric column (1000–50 hPa) and**
 351 **(b) lower troposphere (1000–800 hPa) in March 2010. The purple contours with interval of 0.3 denote AOD differences. Hatching**
 352 **denotes the cloud fraction change is statistically significant at the 95 % confidence level based on Student's *t*-test.**
 353

BB aerosols can dramatically alter the horizontal and vertical distribution of atmospheric temperatures through their radiative effects. Figure 8 shows the spatial pattern of BB aerosol-induced temperature changes from surface to 500 hPa in March 2010. Due to the surface cooling effect of BB aerosols, the surface temperature was reduced by up to 1.6K in the ICP, and the cooling could reach up to 850 hPa (Figs. 8a–b). The BB aerosol-induced warming at 700 hPa can be widely found from the Bay of Bengal across the ICP, SCS and southern China to the East China Sea, with a magnitude between 0.4 and 2.0K (Fig. 8c); and such a warming pattern generally follows the AOD anomaly pattern. As a result, the BB aerosol-induced surface cooling and 700-hPa warming acted to increase the low-level atmospheric stability. Besides, a weak atmospheric cooling effect was found in the mid troposphere (500 hPa) over the ICP (Fig. 8d).

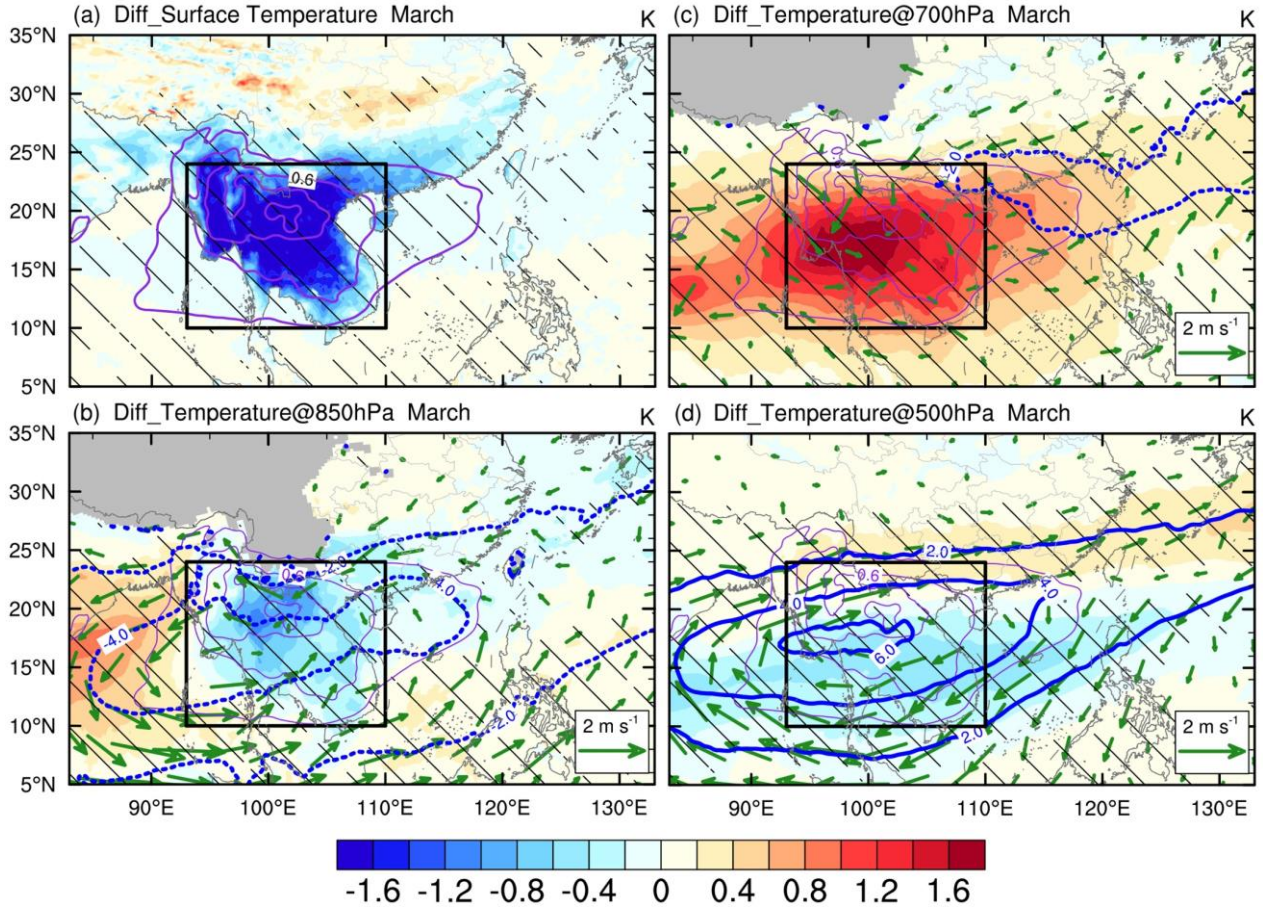
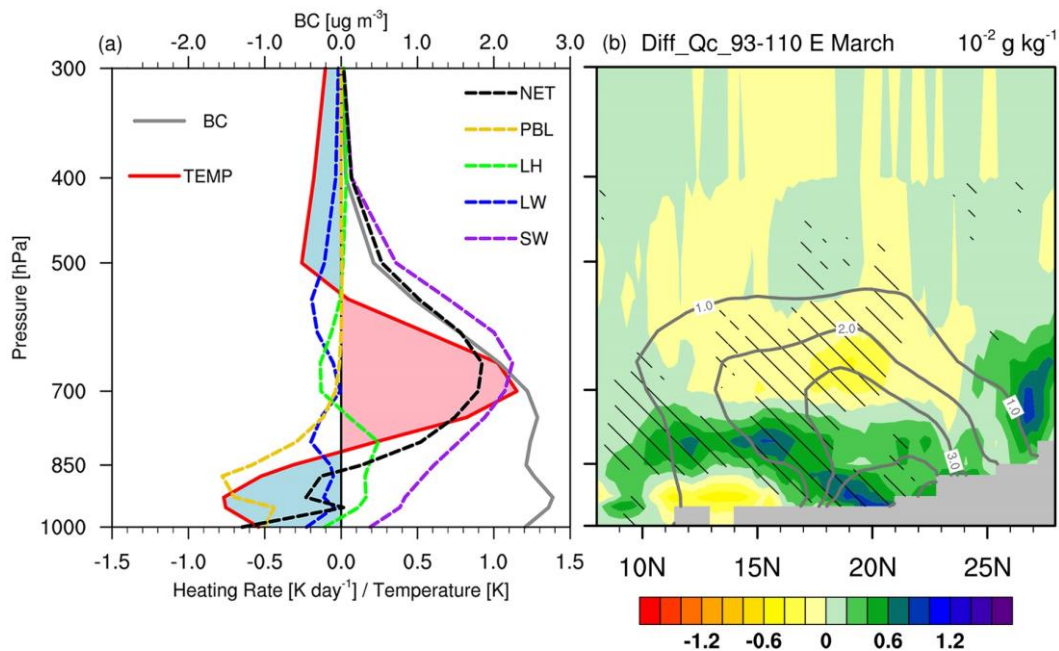


Figure 8: Differences (CTRL minus BBER) in (a) surface temperature (shading; K), (b–d) horizontal wind (vector; m s⁻¹), geopotential height (thick blue contours with interval of 2 dagpm; the dashed contours are for negative values and the zero contour is omitted for clarity), and temperature (shading; K) at (b) 850 hPa, (c) 700 hPa, and (d) 500 hPa in March 2010. Purple contours with interval of 0.3 denote AOD differences. The hatching and green vectors denote temperature and wind changes are statistically significant at the 95 % confidence level, respectively, based on Student's *t*-test. The black box outlines the main Indochina Peninsula (ICP; 93 °–110 °E, 10 °–24 °N).

To better explain such “cooling-warming-cooling” vertical temperature changes from the lower to upper troposphere, we show the vertical profiles of changes in area-averaged atmospheric heating source in the ICP (93 °–110 °E, 10 °–24 °N; black

box in Fig. 8) during March (Fig. 9a). As expected, SW radiative forcing was the major factor contributing to the atmospheric heating, which was the strongest (exceeding 1.0K day^{-1}) near 650 hPa and diminished to zero near 400 hPa. Note that the height of the SW heating did not coincide with that of the BC mass concentration maximum, partially due to the amplification heating effect caused by the increased low-cloud underneath the BB smoke plume (Fig. 9b). The surface cooling caused by the solar flux reduction tends to decrease surface evapotranspiration, and reduce sensible and latent heat fluxes (Andreae et al., 2004; Feingold et al., 2005; Huang et al., 2016b). As a result, the PBL processes dominate the cooling effect in the lower troposphere (1000–700 hPa). This can also explain why the PBL cooling was weaker over the ocean than over land (Figs. 8a–b), as the surface fluxes over the ocean were much less variable (Feingold et al., 2005). The latent heat shows a weak warming effect from ~950 to 750 hPa, which can translate to promoting cloud formation by large-scale condensation and even moist convection. As shown in Figs. 7 and 9b, the increase in low clouds over the Beibu Gulf was concentrated below 850 hPa, while that over the southern ICP was at 850–750 hPa. Additionally, the latent heating also displayed a weak cooling effect at 700–500-hPa because of the reduced clouds in this layer via the cloud burn-off effect of BC (the semi-direct effect). The LW radiative forcing heating contributed to the atmospheric cooling from the surface to about 400 hPa. The net atmospheric heating (i.e., the sum of SW, LW, PBL, and latent heat), induced by BB aerosols generally exhibited a cooling effect below 850 hPa and a warming effect at 850–400 hPa. As a result, the colder temperature anomalies occurred from the surface to 800 hPa with a minimum reaching -0.76K , while warmer anomalies with a maximum greater than 1K were around 800–550 hPa (Fig. 9a). These temperature anomalies can markedly increase the atmospheric stability in the lower troposphere, leading to a more unstable mid troposphere.



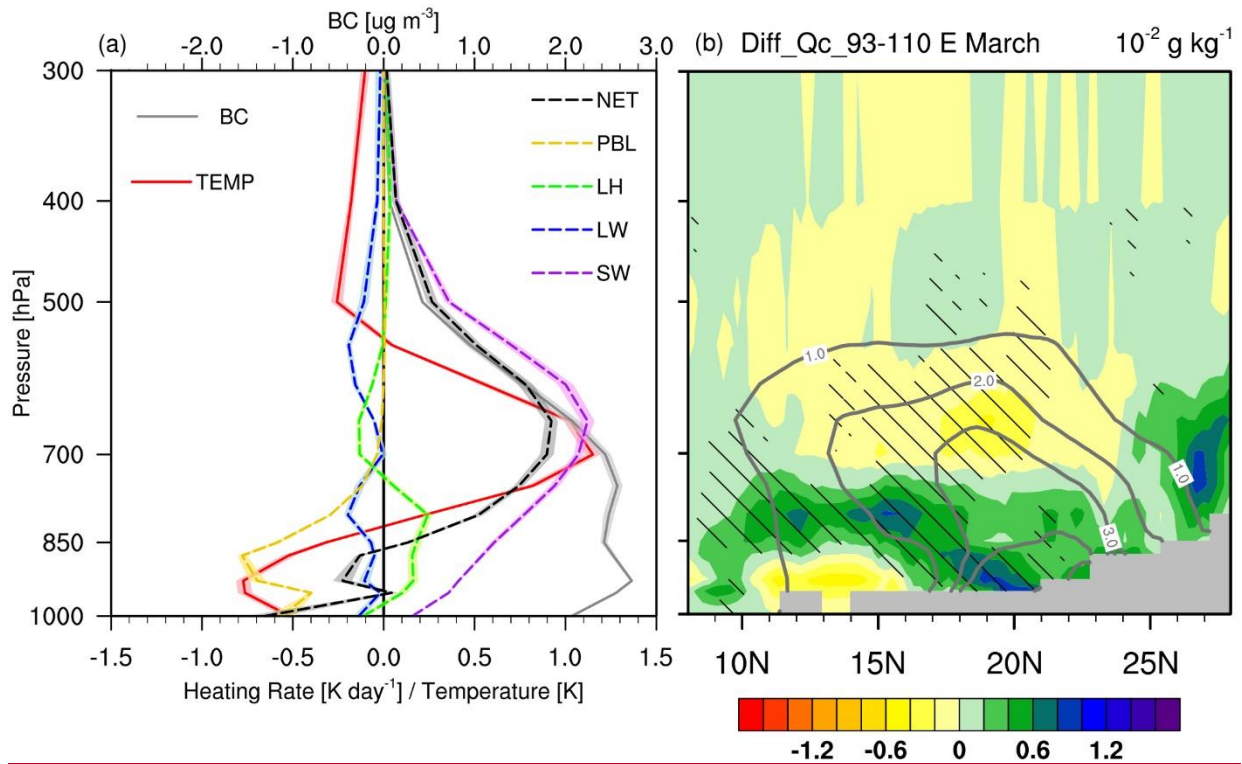
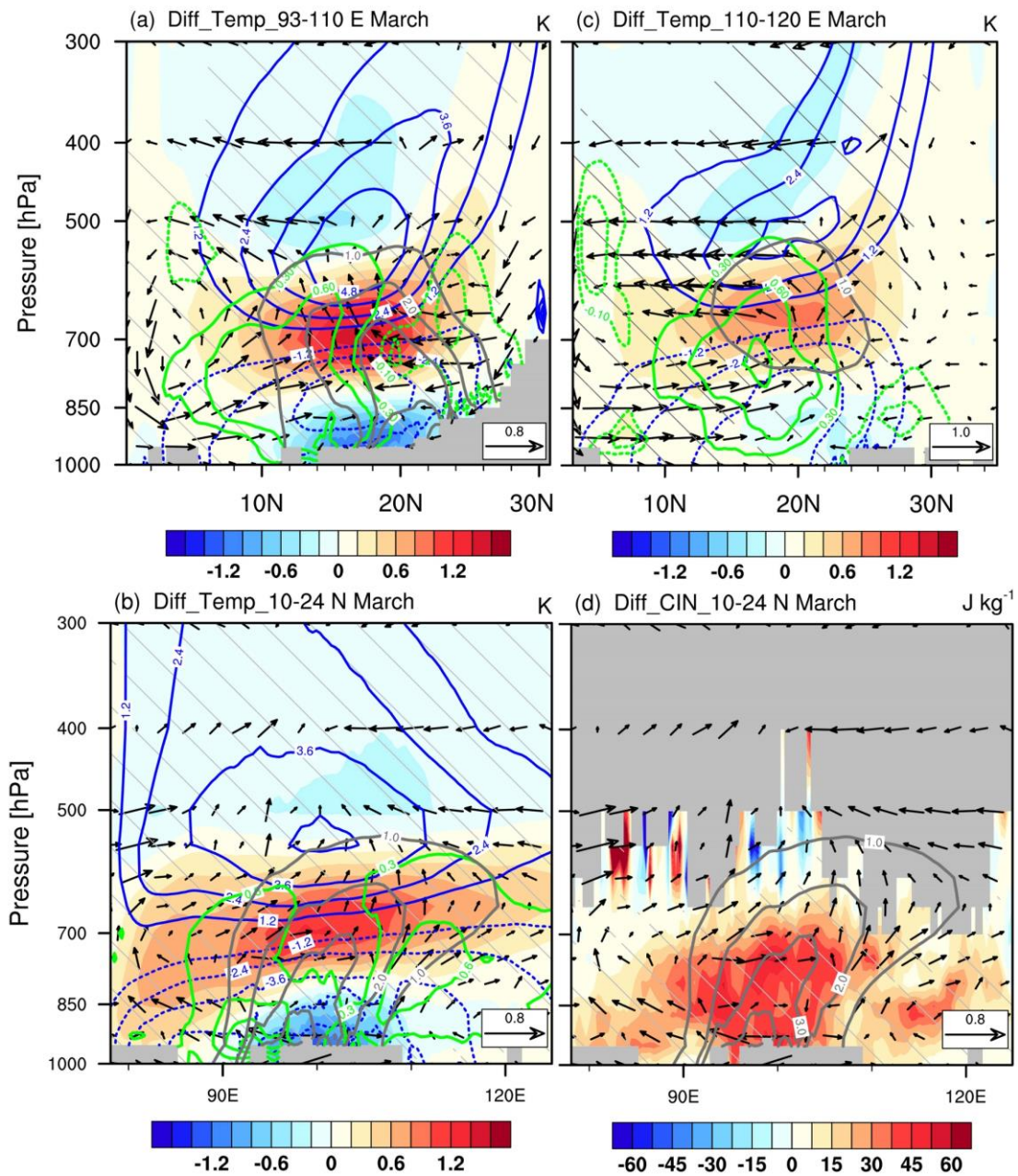


Figure 9: (a) Vertical profiles of differences (CTRL minus BBER) in temperature (solid red line; K), BC mass concentration (solid grey line; ug m^{-3}), and atmospheric heating rates (dashed line; K day^{-1}) averaged over ICP (93 °-110 °E, 10 °-24 °N; as outlined in Fig. 8) in March 2010. Here, atmospheric heating rates include shortwave (SW) and longwave (LW) radiation heating, latent heating (LH; i.e., heating from microphysics and cumulus scheme), and heating from planetary boundary layer (PBL) scheme. Net heating rate (NET) = SW + LW + LH + PBL. (b) Vertical cross-sections of differences (CTRL minus BBER) in cloud water-vapor content (shading; $10^{-2} \text{ g kg}^{-1}$), BC mass concentration (solid grey contours with interval of 1.0 ug m^{-3}) averaged over 93 °-110 °E in March 2010. Shading in (a) denotes a single standard deviation of temperature, BC mass concentration and atmospheric heating rate. Hatching in (b) denotes changes in cloud water-vapor content are statistically significant at the 95 % confidence level based on Student's *t*-test.

The BB aerosol-induced maximum net heating in the troposphere could reach up to 0.9 K day^{-1} (Fig. 9a), which was able to force anomalous atmospheric circulation. As suggested previously (Hoskins, 1991; Wu and Liu, 2000), the atmospheric response to an external diabatic heating can generate upward motion in the heating layer, cyclonic circulation in the lower atmosphere and anticyclonic circulation in the upper troposphere. These anomalous circulations can be clearly seen in our simulation results shown in Figs. 8b–d. Furthermore, subject to atmospheric thermal adaptation (Wu and Liu, 2000; Liu et al., 2001), the “overshooting” air parcel induced by the inertial ascent from below the heating layer kept a constant potential temperature, forming the cold anticyclonic circulation to the northwest of the heat source in the upper troposphere (Figs. 10a – b). Accordingly, anomalous northerly (southerly) winds across the heating region in the upper (lower) troposphere (Fig. 10a) developed to balance the Coriolis force (Liu et al., 2001). To the north of the BB aerosol heating region (22 °– 26 °N), the negative meridional diabatic heating gradient produced a negative vorticity forcing and a secondary circulation at the upper level (Figs. 10a, c). The BB aerosol-induced two-cell structure meridional circulation is quite similar to the results in

411 Lee and Kim (2010) and Yang et al. (2022b). The sinking motion in the northern branch is consistent with the maximum
412 precipitation anomaly in Fig. 5d. The anomalous northwesterly flow on the northern flank of the cyclonic circulation in the
413 lower troposphere substantially weakened the water vapor transported from the Bay of Bengal to the northern ICP and
414 southern China (20 °–30 °N; also see Fig. 10a). However, more water vapor was lifted up from the Bay of Bengal and SCS
415 into the mid troposphere via the Ekman pumping (Fig. 10b), which was partly transported to the central and southern ICP by
416 anomalous southerly wind in the southern branch (Figs. 10a–b). Interestingly, precipitation was reduced in the central and
417 southern ICP by the BB aerosols, despite of the favorable water-vapor condition (Fig. 5d). This is because the increased
418 atmospheric stability in the low-troposphere caused by the BB aerosols greatly enhanced the convection inhibition energy
419 (CIN) (Fig. 10d), indicative of a higher threshold for the energy required to trigger convection (Mapes, 2000). As a result,
420 the reduction of the local convective rainfall dominated the change in precipitation over the ICP (Fig. 11a), while large-scale
421 (stratiform) precipitation presented a minor increase (Fig. 11b). The effects of BB aerosol-induced suppression of convective
422 precipitation and mild enhancement of large-scale precipitation over the northern ICP are consistent with the modelling
423 results of Wang et al. (2021).



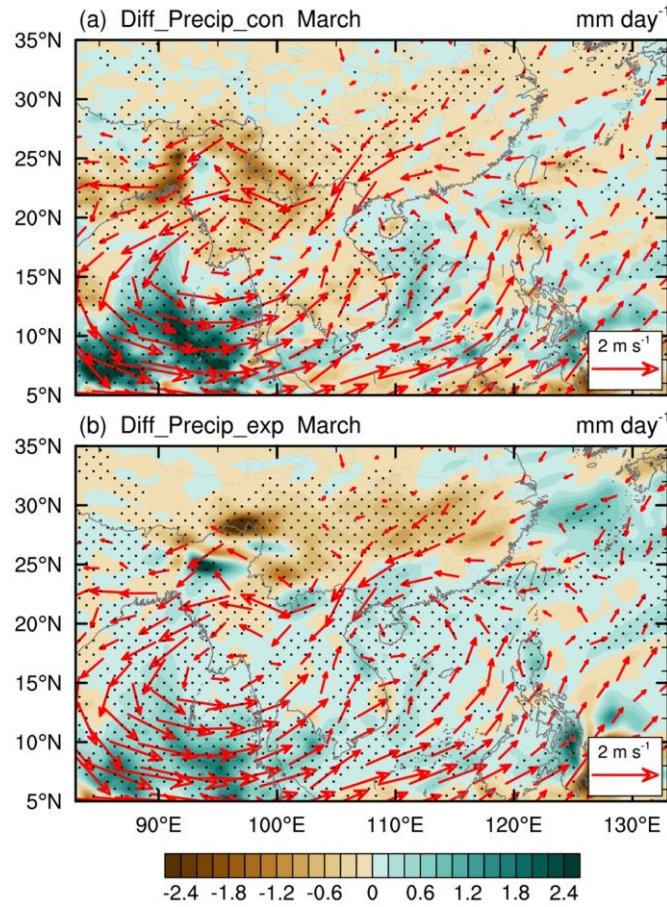


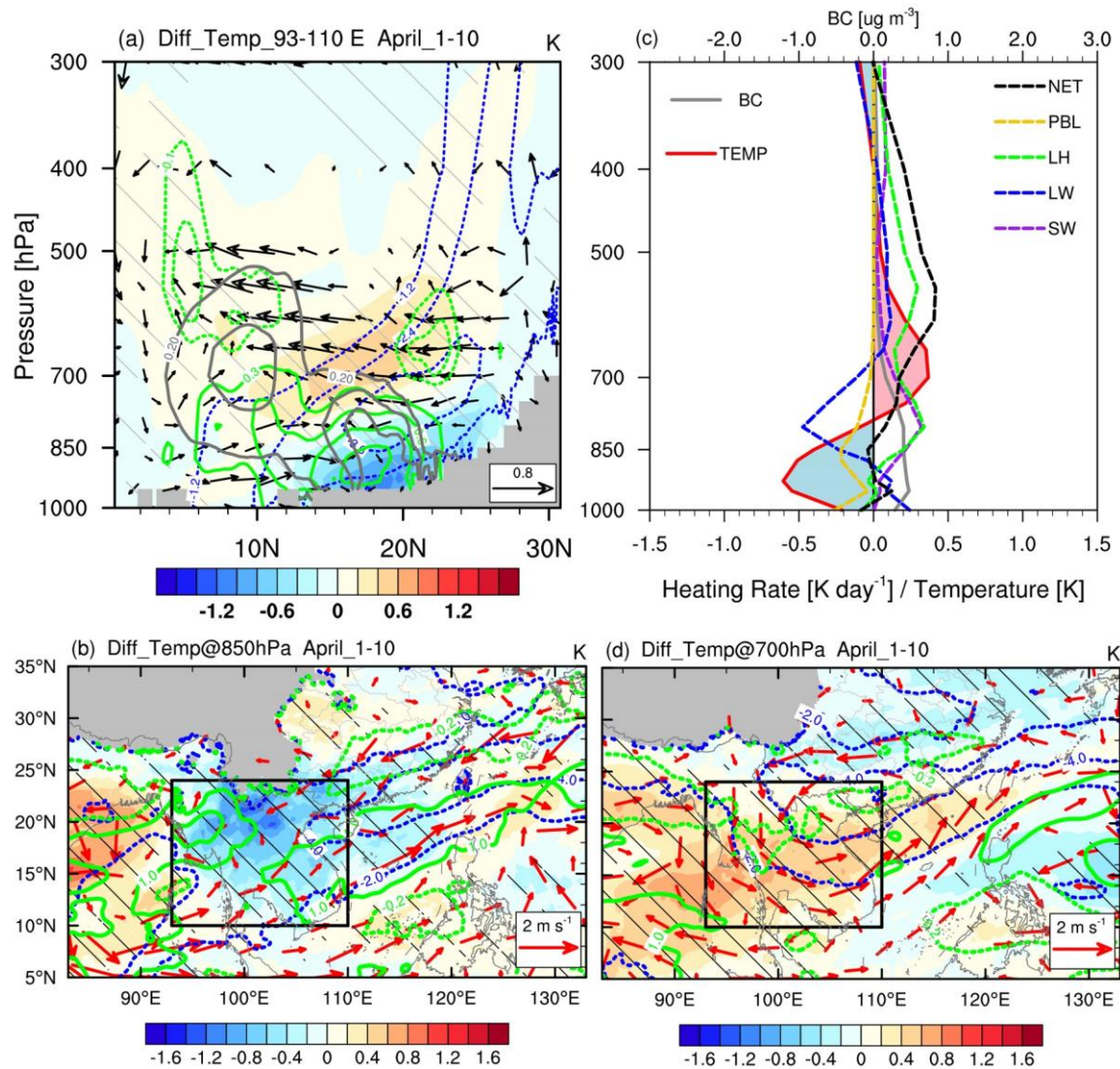
Figure 11: Differences (CTRL minus BBER) in (a) convective precipitation and (b) non-convective precipitation (shading; mm day⁻¹) in March 2010, together with 850-hPa wind difference (vector; m s⁻¹). Stippling and red vector denote precipitation and wind are statistically significant at the 95% confidence level, respectively, based on Student's *t*-test.

For the SCS and its adjacent coastal water region (110°–120°E), the PBL cooling was quite weak (Fig. 10c), resulting in little CIN change in the lower layers (Fig. 10d). Therefore, relatively favorable water-vapor conditions led to moderately enhanced precipitation (Fig. 5d). This is similar to the “elevated heat pump” (EHP) effect proposed by Lau et al. (2006), which hypothesized that the absorbing aerosols (dust and BC) stacked up on the southern slope of the Tibetan Plateau can heat up the mid-to-upper troposphere, leading to an earlier onset of the Indian summer monsoon and increased monsoon rainfall. Note that in our case the updraft caused by the low-level (700-hPa) heating only reached 500 hPa, leading to an invigoration of shallow convection, which differs from the original “EHP” effect with a high-level (500-hPa) heating and a resultant ascent air flow reaching 200 hPa.

4.3.2 Delayed effect

Compared to the instant effect, the delayed effect in the subsequent April should be closely related to the atmospheric circulation adjustment, as there were a few BB aerosols left from March. During the subsequent early-April, the anomalous

vertical temperature structure still persisted with a maximum warming of 0.4K at 700 hPa and cooling of -0.6K at 925 hPa (Figs. 12a, c). Without the strong heating from the BB aerosols (Fig. 12c), the 850-hPa anomalous low over the ICP became weaker and split into a double-center system (Fig. 12b). This would increase moisture over the northern ICP and northern SCS by southerly anomalies, which facilitated precipitation over the northern ICP, southern China and the northern SCS (Figs. 12b, d and Fig. 5e).



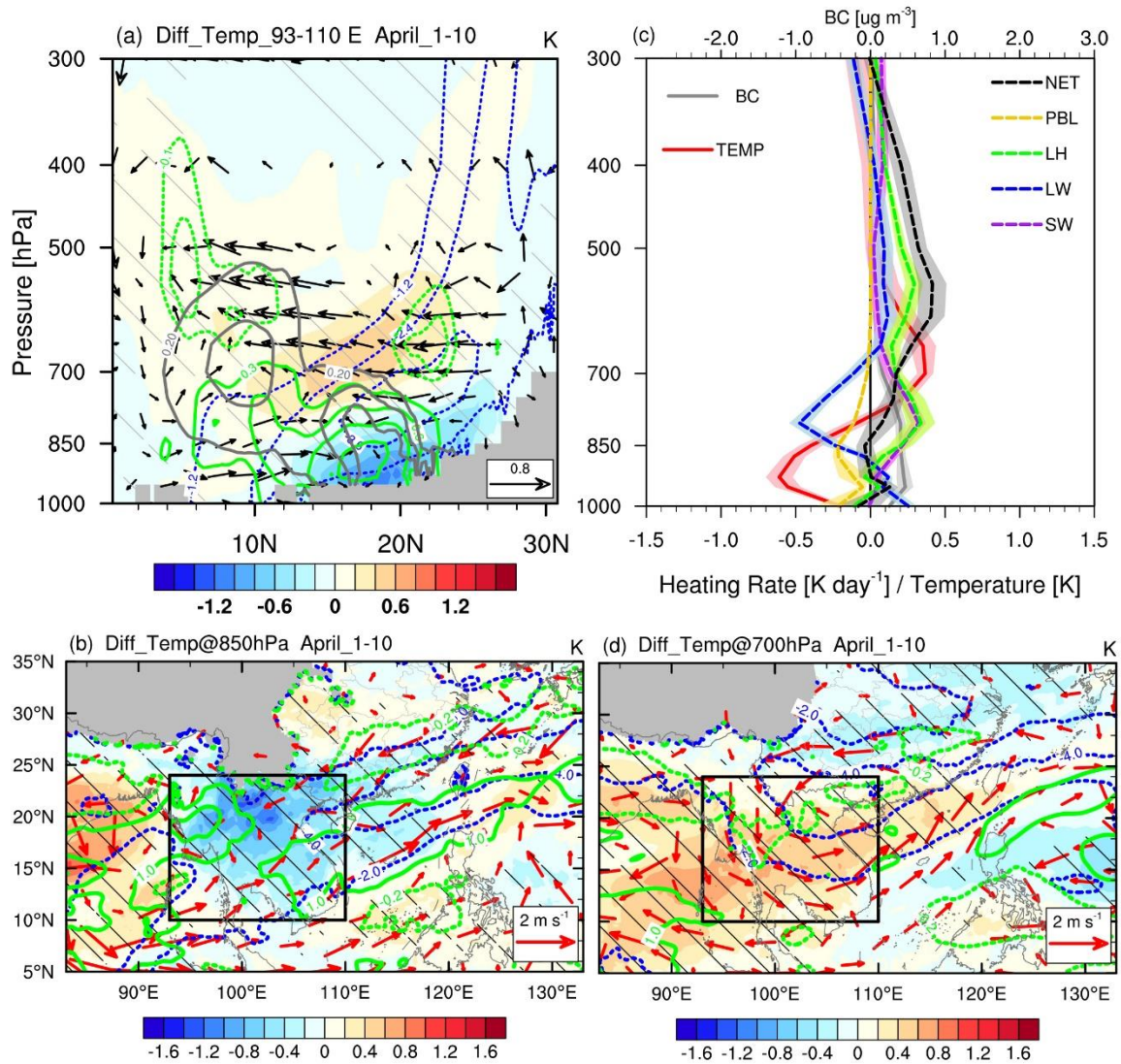
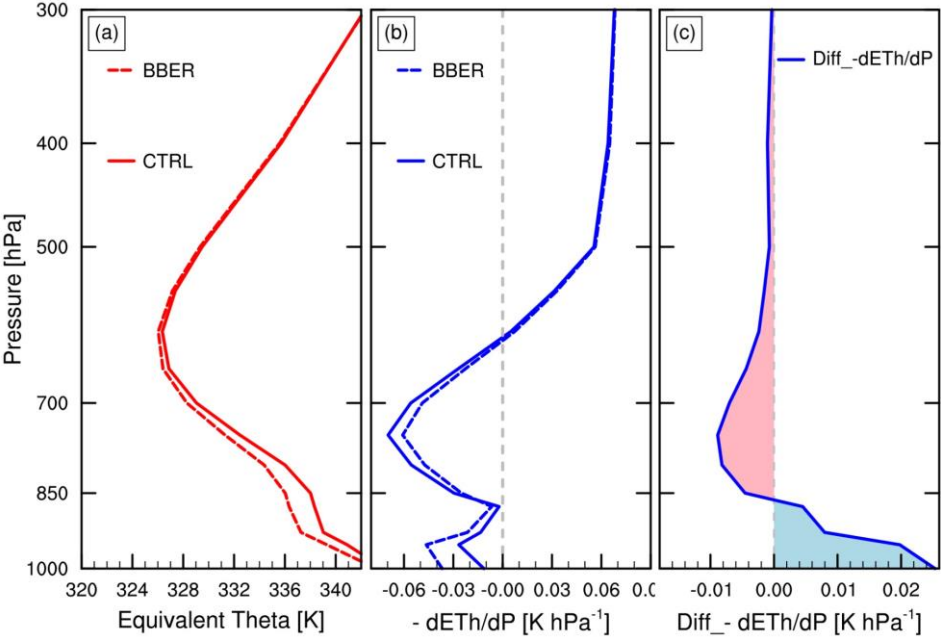


Figure 12: (a) Vertical cross-sections of differences (CTRL minus BBER) in temperature (shading; K), geopotential height (blue contours with interval of 1.2 dagpm; the dashed contours are for negative values, and the zero contour is omitted for clarity), and water-vapor content (green contours with interval of 0.3 g kg⁻¹ for positive values and of 0.1 g kg⁻¹ for negative values, and the zero contour is omitted for clarity), together with meridional and vertical velocity (vector; m s⁻¹ and 10⁻² m s⁻¹, respectively) and BC mass concentration (solid grey contours with interval of 0.2 ug m⁻³) averaged over 93–110 E. (b) Differences (CTRL minus BBER) in 850-hPa wind (vector; m s⁻¹), geopotential height (blue contours with interval of 1.2 dagpm), water-vapor content (green contours with interval of 1.0 g kg⁻¹ for positive values and of 0.2 g kg⁻¹ for negative values, and the zero contour is omitted for clarity), and temperature (shading; K). (c) Vertical profiles of differences (CTRL minus BBER) in temperature (solid red line; K), BC mass concentration (solid grey line; ug m⁻³), and atmospheric heating rates (dashed lines; K day⁻¹) averaged over the ICP [black box in (b)]. (d) Same as (b), but at 700 hPa. Shading in (c) denotes a single standard deviation of temperature, BC mass concentration and atmospheric heating rate. Hatching and vector denote the shaded field and wind changes are statistically significant at the 95 % confidence level, respectively, based on Student's *t*-test. All of them are averaged over April 1st–10th, 2010 (i.e., early-April).

468 As analyzed in Sect. 4.3.1, the rainfall reduction over the ICP in March induced by BB aerosols resulted from competition
 469 between convection suppression by the stabilized atmosphere and favorable water vapor-conditions by large-scale
 470 circulation response. For the delayed effect in early-April, favorable water-vapor conditions due to atmospheric circulation
 471 adjustments increased significantly, as the low-level anomalous low weakened and the monsoon advanced. On the other
 472 hand, the convective instability above 850 hPa was significantly enhanced under the influence of water vapor (Fig. 13c),
 473 although the BB aerosol-induced anomalous vertical temperature structure remained. In other words, both conditions were
 474 conducive to the precipitation over the ICP in the early-April. Thus, the delayed effect acted to promote precipitation over
 475 the ICP, in contrast to inhibiting precipitation by the instant effects. In turn, the increased condensation heating associated
 476 with increased rainfall dominated the upper-air diabatic heating (Fig. 12c) via positive feedback. The adjustment in the net
 477 maximum heating layer height also led to an anomalous cyclonic circulation at 700 hPa (Fig. 12d). Due to the memory of the
 478 soil, the reduction in land surface variables such as soil temperature, soil moisture and surface evaporation can last until this
 479 period and keep the cooling effect through the PBL process (Fig. 12c). Then, all these factors acted to maintain the
 480 anomalous vertical structure of PBL cooling, upper-air warming and the anomalous circulation, so that the preceding
 481 atmospheric responses would not disappear immediately.



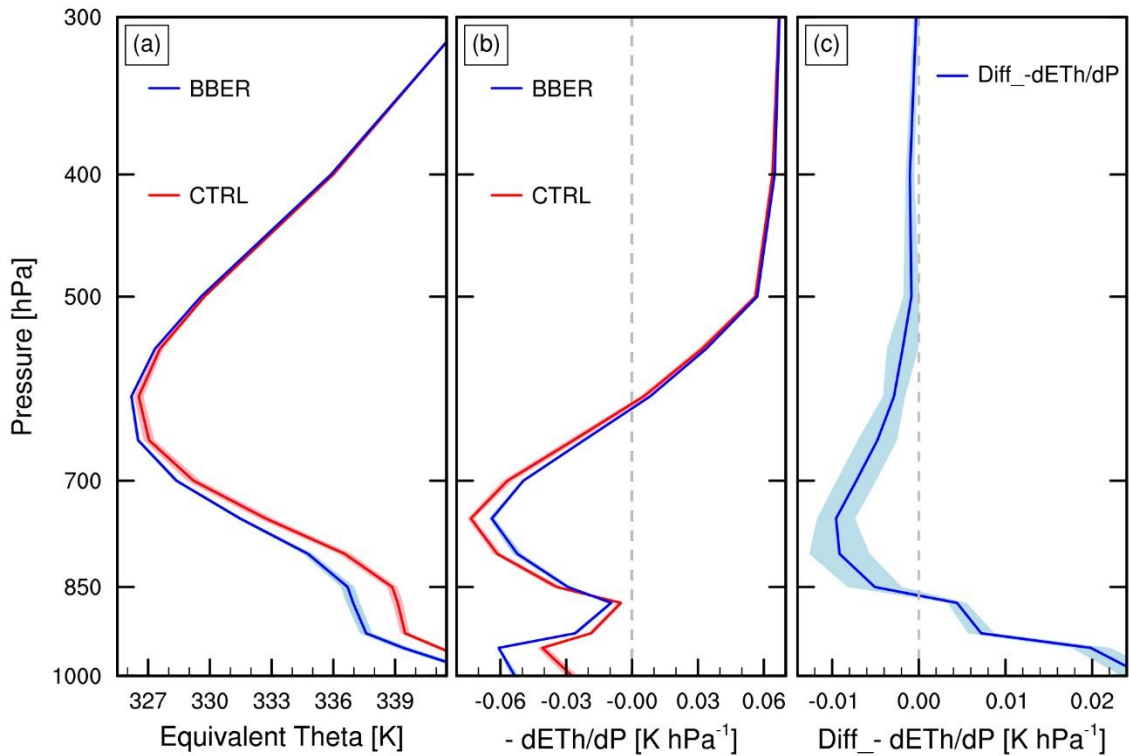
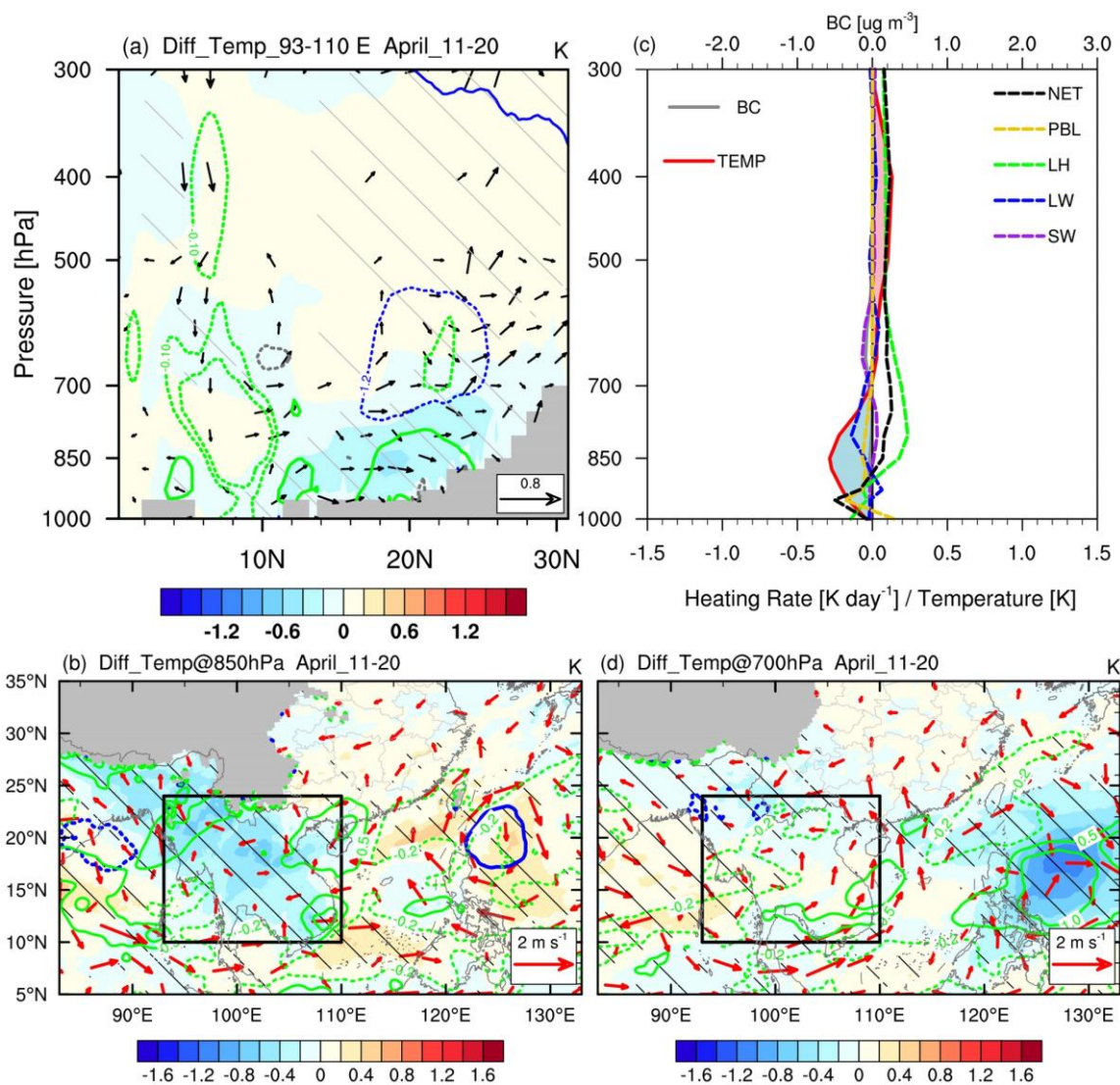


Figure 13: Vertical profiles of (a) equivalent potential temperature (θ_e ; red line; K) and (b) convective stability ($-\frac{\partial \theta_e}{\partial p}$; blue line; K hPa^{-1}) averaged over the ICP (as outlined in Fig. 12b) during April 1st-10th, 2010. The solid red and blue curves are for CTRL and BBER, respectively. (c) Differences (CTRL minus BBER) in the convective stability (blue curve; K hPa^{-1}). Shading denotes a single standard deviation of equivalent potential temperature, convective stability and differences in convective stability.

Without the anomalous heating from the BB aerosols during the mid-April, the anomalous vertical temperature structure was barely seen over the ICP (Figs. 14a, c). Meanwhile, as the 850-hPa anomalous low further dissipated, anomalous southerly wind transported more water vapor from the Bay of Bengal directly northward to the northwestern ICP (Fig. 14b). The moist airflows were then lifted by the southeastern Tibetan Plateau and thus converged and cooled, which enhanced orographic precipitation (Fig. 5f). Although the BB aerosol-induced anomalous low nearly disappeared over coastal Southeast China during the mid-April, the anomalous meridional circulation accompanied by enhanced precipitation over southern China (Fig. 5f) could be sustained through the feedback from the increased condensation heating.



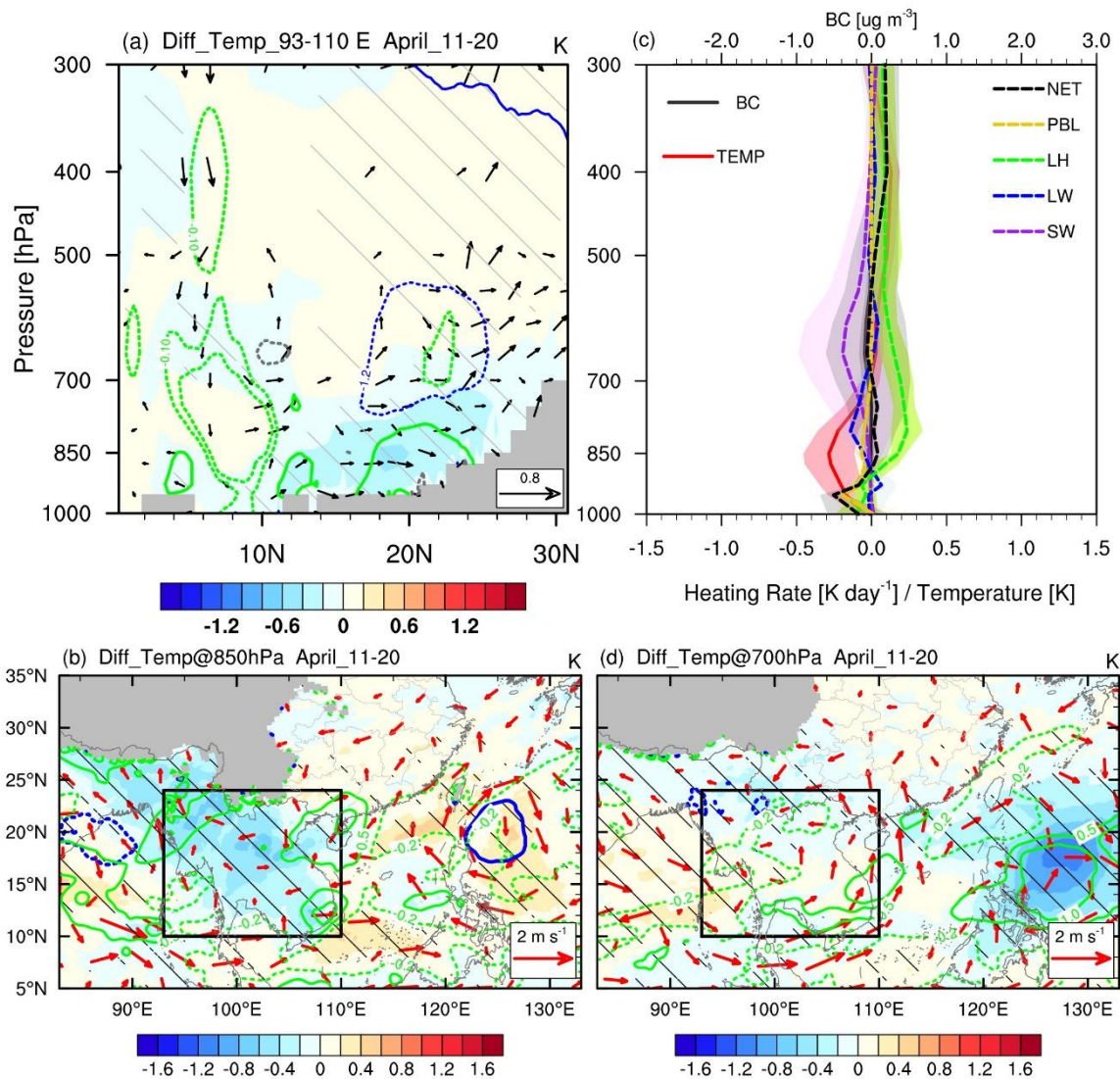


Figure 14: Same as Fig. 12, but the field are averaged over April 11th-20th, 2010 (i.e., mid-April).

5 Conclusions and discussion

Large amounts of absorbing aerosols are injected into the atmosphere by extensive BB activities over the ICP during March, which can significantly affect the regional climate. Using observation data and the WRF-Chem model, we investigate the instant and delayed effects of the BB aerosols over the ICP in March on the regional circulation and precipitation in early-spring. The main conclusions are summarized below.

The observations show that March BB aerosols are negatively correlated with the rainfall over the ICP, while such a correlation shifts to be positive in early- and mid-April, which is well captured by the WRF-Chem model. The simulation

505 results reveal that BB aerosols emitted from the northern ICP trap a substantial proportion of solar radiation in the low-to-
 506 mid troposphere and decrease incoming solar radiation at the surface, followed by reduced surface heat fluxes associated
 507 with PBL processes. The energy perturbation leads to temperature changes in surface and lower tropospheric (1000–850-hPa)
 508 cooling and lower-to-mid tropospheric (850–400-hPa) heating. Thus, the low atmosphere is stabilized and CIN is markedly
 509 intensified at 850–700 hPa, which acts to suppress local convective rainfall. The BB aerosol-induced heating in the low-to-
 510 mid troposphere can also cause an anomalous low-pressure system in the lower troposphere extending from the central Bay
 511 of Bengal across the ICP to the northern SCS. This is accompanied by a two-cell structure meridional circulation with rising
 512 motion over the ICP and two strong downward motions in the near-equatorial regions and the latitudes of 25 °–30 °N. Over
 513 the ICP, the anomalous low in the lower troposphere tends to increase the mid-tropospheric moisture from the Bay of Bengal
 514 and SCS via moisture advection and Ekman pumping. On the southern flank of this anomalous low, the southerly wind
 515 conveys more water vapor to the ICP, causing a minor increase in large-scale precipitation. Thus, the BB aerosol-induced
 516 rainfall suppression in the ICP during March is a result of competition between the responses of local atmospheric stability
 517 and large-scale circulation to absorbing aerosols. For the SPRJ region, the anomalous northeasterly wind on the northern
 518 flank of the anomalous low would decrease the prevailing southwesterly wind and moisture transport, which is conducive to
 519 suppress the rainfall over these regions. Meanwhile, the sinking motion in the northern branch of anomalous two-cell
 520 structure meridional circulation induced by BB aerosols would also help reduce the precipitation there. Over the SCS, the
 521 moderate precipitation increase is due to favorable water-vapor conditions, while the CIN increases very little because of the
 522 insignificant PBL cooling, which is caused by the underlying water surface.

523 During early-April, the anomalous belt-shaped low-pressure weakens and fragments into a double-center system, owing to a
 524 few BB aerosols remaining in March and the corresponding reduction in BB aerosol-induced atmospheric heating. Over the
 525 ICP, although the anomalous low weakens due to lack of strong heating from the BB aerosols, it can still transport sufficient
 526 moisture from the Bay of Bengal as the monsoon advances. On the other hand, the convective instability above 850 hPa is
 527 enhanced under the influence of water vapor, although the vertical temperature anomaly structure remains. As a result, the
 528 effects of March BB aerosols on precipitation over the ICP shift from suppression in March to enhancement in early- and
 529 mid-April. In turn, the increased condensation heating associated with increased rainfall dominates the diabatic heating and
 530 sustains the anomalous circulation and vertical temperature structure via positive feedback. In mid-April, without any
 531 anomalies directly related to BB aerosol-induced heating, the anomalous vertical temperature structure and low pressure in
 532 the lower troposphere nearly disappear, and only enhanced rainfall over the northwestern ICP and southern China can be
 533 seen due to the condensation heating.

534 Recently, Yang et al. (2022b) investigated the effects of BB aerosols from the ICP during the whole emission season (March
 535 1st–April 17th, 2010). In this study, we further discuss the instant and delayed effects in the peak BB emission month of
 536 March. The instant effect of March BB aerosols on the atmospheric circulation is consistent with the results of Yang et al.
 537 (2022b). Interestingly, Yang et al. (2022b) noted that the April BB aerosols could significantly enhance the heavy rain events
 538 over the southern coast of southern China, while we show that the BB aerosol perturbation in March can induce a delayed

539 increase in April precipitation over the same region. For the precipitation decrease over southern China, in addition to the
540 cyclonic anomalies that reduce water vapor transport as stated by Yang et al. (2022b), we find that the sinking motion in the
541 anomalous vertical meridional circulation induced by BB aerosol's heating also plays a role. Using an AGCM, Lee et al.
542 (2014) suggested that the indirect effect is the main contributor to the BB aerosol-induced precipitation suppression over the
543 ICP. In contrast, Ding et al. (2021) demonstrated that the indirect effects of BB aerosols play a less significant role in the
544 low-cloud enhancement over subtropical Asia. Although both direct and indirect effects of aerosols are included in our
545 experiments, we focus on the aerosol-radiation interaction (i.e., direct or semi-direct effect). The role of indirect effects
546 needs to be investigated by setting up experiments with and without indirect effects in further.

547 It is worth noting that this study examines the BB aerosol climate effects using the model by reducing BB emission, while
548 another method is commonly used, namely, by turning on and off the aerosol climate feedback configuration (e.g., Ding et
549 al., 2021; Wang et al., 2021). We have done a simple verification, and found that the results obtained by the two methods are
550 similar (Fig. S2). Additionally, although some quantitative results can be derived in this study, such as a 12.94(± 4.22)%
551 reduction (the value after “ \pm ” is a single standard deviation, hereafter the same) in rainfall in the ICP (92°–108°E, 12°–27°N)
552 due to March BB aerosols' instant effect, and 15.40(± 5.11)% and 13.93(± 5.65)% enhancements from the delayed effect in
553 early- and mid-April, respectively, these quantitative results would rely on the BB emission reduction rate in the sensitivity
554 experiment. A supplementary sensitivity test with 50% BB emission showed that the anomalous patterns of 850-hPa wind
555 and rainfall are quite similar to those from BBER, but the rainfall anomalies are 72.73%, 36.15% and 31.50% of those from
556 BBER in March, early- and mid-April, respectively (Fig. S3), indicating our qualitative conclusions are robust. As for
557 quantitative results, this study is based on preliminary analysis; more experiments with different BB emission scenarios need
558 to be designed to obtain more precise results in the future.

559 Note that the modeling results in this study focuses only on the year of 2010, during which the AOD magnitude in March
560 was above the average greater than its climatology by about 1.7 standard deviations. The effects of aerosols on precipitation
561 in the model (Figs. 5d–f) are not fully consistent with observations (Figs. 3d–f), especially for the delayed effects (Figs. 3e, f
562 and Figs. 5e, f). Due to the fact that the response patterns of large-scale circulation and precipitation to BB aerosols largely
563 depend on both aerosols and meteorological conditions. Thus, multiyear simulations are needed to assess the robustness of
564 our results on a longer time scale. In addition, uncertainty may also exist in the simulation. For instance, the overestimate of
565 convective rainfall in the tropical Bay of Bengal and orographic precipitation in the southeastern Tibetan Plateau might
566 introduce some uncertainty in the response of large-scale circulation to BB aerosols, which is strongly related to the cumulus
567 convection parameterization scheme and the topographic complexity (Ma and Tan, 2009; Li et al., 2022). Therefore, further
568 experiments at convection-resolved resolution need to be conducted to reduce such uncertainty.

569 **Code and Data availability.**

570 The source codes of WRF-Chem model are available at https://www2.mmm.ucar.edu/wrf/users/download/get_source.html.
571 The FNL data are available at <https://rda.ucar.edu/datasets/ds083.2/>. The BB emission data of FINN version 1.5 are available
572 at <https://www.acom.ucar.edu/Data/fire/>. The MEIC and MIX anthropogenic emissions are available at
573 http://meicmodel.org/?page_id=541&lang=en. The ERA-5 Reanalysis data are available at
574 <https://cds.climate.copernicus.eu/cdsapp#!/search?type=dataset>. MERRA-2 aerosol reanalysis data, OMI AI and TRMM
575 precipitation are available at <https://disc.gsfc.nasa.gov/datasets>. The MODIS AOD are available at
576 https://ladsweb.modaps.eosdis.nasa.gov/missions-and-measurements/products/MOD08_M3. The BB emission data of
577 GFEDv4 are available at https://daac.ornl.gov/VEGETATION/guides/fire_emissions_v4_R1.html.

578 **Author contributions.**

579 HX and AZ conceptualized the research goals and aims. SH and AZ ran the simulations. AZ performed the data analysis and
580 visualized the results. AZ, HX, JD, and JM wrote the initial draft.

581 **Acknowledgments**

582 This work is jointly supported by the National Natural Science Foundation of China (41975106 and 42192562). We
583 acknowledge the High Performance Computing Center of Nanjing University of Information Science & Technology for their
584 support of this work. We also thank all the corresponding institutions for providing their data for this study.

585 **Competing interests**

586 The authors declare that they have no conflict of interest.

587 **Financial support**

588 This research has been supported by the National Natural Science Foundation of China (41975106 and 42192562).

589 **References**

590 Adam, M. G., Tran, P. T. M., Bolan, N., and Balasubramanian, R.: Biomass burning-derived airborne particulate matter in
591 Southeast Asia: A critical review, J. Hazard. Mater., 407, 124760, <https://doi.org/10.1016/j.jhazmat.2020.124760>, 2021.

592 Andreae, M. O., Rosenfeld, D., Artaxo, P., Costa, A. A., Frank, G. P., Longo, K. M., and Silva-Dias, M. A. F.: Smoking rain
593 clouds over the Amazon, *Sci.*, 303, 1337-1342, 10.1126/science.1092779, 2004.

594 Argüeso, D., Hidalgo-Muñoz, J. M., Gámiz-Fortis, S. R., Esteban-Parra, M. J., and Castro-Díez, Y.: High-resolution
595 projections of mean and extreme precipitation over Spain using the WRF model (2070–2099 versus 1970–1999), *J. Geophys.*
596 *Res.-Atmos.*, 117, <https://doi.org/10.1029/2011JD017399>, 2012.

597 Ban-Weiss, G. A., Cao, L., Bala, G., and Caldeira, K.: Dependence of climate forcing and response on the altitude of black
598 carbon aerosols, *Clim. Dynam.*, 38, 897-911, 10.1007/s00382-011-1052-y, 2012.

599 Bao, Z., Wen, Z., and Wu, R.: Variability of aerosol optical depth over east Asia and its possible impacts, *J. Geophys. Res.-*
600 *Atmos.*, 114, 10.1029/2008jd010603, 2009.

601 Bohren, C. F., and Huffman, D. R.: Absorption and scattering of light by small particles, John Wiley & Sons, New York,
602 1983.

603 Bond, T. C., Streets, D. G., Yarber, K. F., Nelson, S. M., Woo, J.-H., and Klimont, Z.: A technology-based global inventory
604 of black and organic carbon emissions from combustion, *J. Geophys. Res.-Atmos.*, 109,
605 <https://doi.org/10.1029/2003JD003697>, 2004.

606 Buchard, V., Randles, C. A., Silva, A. M. d., Darmenov, A., Colarco, P. R., Govindaraju, R., Ferrare, R., Hair, J., Beyersdorf,
607 A. J., Ziemba, L. D., and Yu, H.: The MERRA-2 aerosol reanalysis, 1980 onward. Part II: Evaluation and case studies, *J.*
608 *Climate*, 30, 6851-6872, 10.1175/jcli-d-16-0613.1, 2017.

609 Caldwell, P., Chin, H.-N. S., Bader, D. C., and Bala, G.: Evaluation of a WRF dynamical downscaling simulation over
610 California, *Climatic Change*, 95, 499-521, 10.1007/s10584-009-9583-5, 2009.

611 Chand, D., Wood, R., Anderson, T. L., Satheesh, S. K., and Charlson, R. J.: Satellite-derived direct radiative effect of
612 aerosols dependent on cloud cover, *Nat. Geosci.*, 2, 181-184, 10.1038/ngeo437, 2009.

613 Chavan, P., Fadnavis, S., Chakroborty, T., Sioris, C. E., Griessbach, S., and Müller, R.: The outflow of Asian biomass
614 burning carbonaceous aerosol into the upper troposphere and lower stratosphere in spring: radiative effects seen in a global
615 model, *Atmos. Chem. Phys.*, 21, 14371-14384, 10.5194/acp-21-14371-2021, 2021.

616 Chen, Y., Yang, K., Zhou, D., Qin, J., and Guo, X.: Improving the Noah land surface model in arid regions with an
617 appropriate parameterization of the thermal roughness length, *J. Hydrol.*, 11, 995-1006, 10.1175/2010jhm1185.1, 2010.

618 de Graaf, M., Stammes, P., Torres, O., and Koelemeijer, R. B. A.: Absorbing Aerosol Index: Sensitivity analysis, application
619 to GOME and comparison with TOMS, *J. Geophys. Res.-Atmos.*, 110, <https://doi.org/10.1029/2004JD005178>, 2005.

620 Deng, X., Tie, X., Zhou, X., Wu, D., Zhong, L., Tan, H., Li, F., Huang, X., Bi, X., and Deng, T.: Effects of Southeast Asia
621 biomass burning on aerosols and ozone concentrations over the Pearl River Delta (PRD) region, *Atmos. Environ.*, 42, 8493-
622 8501, <https://doi.org/10.1016/j.atmosenv.2008.08.013>, 2008.

623 Ding, K., Huang, X., Ding, A., Wang, M., Su, H., Kerminen, V.-M., Petäjä T., Tan, Z., Wang, Z., Zhou, D., Sun, J., Liao, H.,
624 Wang, H., Carslaw, K., Wood, R., Zuidema, P., Rosenfeld, D., Kulmala, M., Fu, C., Pöschl, U., Cheng, Y., and Andreae, M.

625 O.: Aerosol-boundary-layer-monsoon interactions amplify semi-direct effect of biomass smoke on low cloud formation in
626 Southeast Asia, *Nat. Commun.*, 12, 6416, 10.1038/s41467-021-26728-4, 2021.

627 Dong, X., Fu, J. S., Huang, K., Zhu, Q., and Tipton, M.: Regional climate effects of biomass burning and dust in East Asia:
628 Evidence from modeling and observation, *Geophys. Res. Lett.*, 46, 11490-11499, 10.1029/2019gl083894, 2019.

629 Feingold, G., Jiang, H., and Harrington, J. Y.: On smoke suppression of clouds in Amazonia, *Geophys. Res. Lett.*, 32,
630 <https://doi.org/10.1029/2004GL021369>, 2005.

631 Gautam, R., Hsu, N. C., Eck, T. F., Holben, B. N., Janjai, S., Jantarach, T., Tsay, S.-C., and Lau, W. K.: Characterization of
632 aerosols over the Indochina peninsula from satellite-surface observations during biomass burning pre-monsoon season,
633 *Atmos. Environ.*, 78, 51-59, <https://doi.org/10.1016/j.atmosenv.2012.05.038>, 2013.

634 Gelaro, R., McCarty, W., Suárez, M. J., Todling, R., Molod, A., Takacs, L., Randles, C. A., Darmenov, A., Bosilovich, M.
635 G., Reichle, R., Wargan, K., Coy, L., Cullather, R., Draper, C., Akella, S., Buchard, V., Conaty, A., da Silva, A. M., Gu, W.,
636 Kim, G.-K., Koster, R., Lucchesi, R., Merkova, D., Nielsen, J. E., Partyka, G., Pawson, S., Putman, W., Rienecker, M.,
637 Schubert, S. D., Sienkiewicz, M., and Zhao, B.: The modern-era retrospective analysis for research and applications, version
638 2 (MERRA-2), *J. Climate*, 30, 5419-5454, 10.1175/jcli-d-16-0758.1, 2017.

639 Gonçalves, W. A., Machado, L. A. T., and Kirstetter, P. E.: Influence of biomass aerosol on precipitation over the Central
640 Amazon: an observational study, *Atmos. Chem. Phys.*, 15, 6789-6800, 10.5194/acp-15-6789-2015, 2015.

641 Grell, G. A., and Freitas, S. R.: A scale and aerosol aware stochastic convective parameterization for weather and air quality
642 modeling, *Atmos. Chem. Phys.*, 14, 5233-5250, 10.5194/acp-14-5233-2014, 2014.

643 Guenther, A. B., Jiang, X., Heald, C. L., Sakulyanontvittaya, T., Duhl, T., Emmons, L. K., and Wang, X.: The model of
644 emissions of gases and aerosols from nature version 2.1 (MEGAN2.1): an extended and updated framework for modeling
645 biogenic emissions, *Geosci. Model Dev.*, 5, 1471-1492, 10.5194/gmd-5-1471-2012, 2012.

646 Gupta, P., Levy, R. C., Mattoo, S., Remer, L. A., and Munchak, L. A.: A surface reflectance scheme for retrieving aerosol
647 optical depth over urban surfaces in MODIS Dark Target retrieval algorithm, *Atmos. Meas. Tech.*, 9, 3293-3308,
648 10.5194/amt-9-3293-2016, 2016.

649 Heidinger, A. K., Foster, M. J., Walther, A., and Zhao, X.: The pathfinder atmospheres–extended AVHRR climate dataset, *B.*
650 *Am. Meteorol. Soc.*, 95, 909-922, 10.1175/bams-d-12-00246.1, 2014.

651 Herbert, R., Stier, P., and Dagan, G.: Isolating large-scale smoke impacts on cloud and precipitation processes over the
652 Amazon with convection permitting resolution, *J. Geophys. Res.-Atmos.*, 126, e2021JD034615,
653 <https://doi.org/10.1029/2021JD034615>, 2021.

654 Hersbach, H., and Dee, D.: ERA5 reanalysis is in production, *ECMWF newsletter*, 147, 5-6, 2016.

655 Hodnebrog, Ø., Myhre, G., Forster, P. M., Sillmann, J., and Samset, B. H.: Local biomass burning is a dominant cause of the
656 observed precipitation reduction in southern Africa, *Nat. Commun.*, 7, 11236, 10.1038/ncomms11236, 2016.

657 Holben, B. N., Eck, T. F., Slutsker, I., Tanré D., Buis, J. P., Setzer, A., Vermote, E., Reagan, J. A., Kaufman, Y. J.,
 658 Nakajima, T., Lavenu, F., Jankowiak, I., and Smirnov, A.: AERONET—A federated instrument network and data archive
 659 for aerosol characterization, *Remote. Sens. Environ.*, 66, 1-16, [https://doi.org/10.1016/S0034-4257\(98\)00031-5](https://doi.org/10.1016/S0034-4257(98)00031-5), 1998.
 660 Hoskins, B. J.: Towards a PV- θ view of the general circulation, *Tellus A*, 43, 27-36, 10.3402/tellusa.v43i4.11936, 1991.
 661 Huang, H.-Y., Wang, S.-H., Huang, W.-X., Lin, N.-H., Chuang, M.-T., da Silva, A. M., and Peng, C.-M.: Influence of
 662 synoptic-dynamic meteorology on the long-range transport of Indochina biomass burning aerosols, *J. Geophys. Res.-Atmos.*,
 663 125, e2019JD031260, <https://doi.org/10.1029/2019JD031260>, 2020.
 664 Huang, K., Fu, J. S., Hsu, N. C., Gao, Y., Dong, X., Tsay, S.-C., and Lam, Y. F.: Impact assessment of biomass burning on
 665 air quality in Southeast and East Asia during BASE-ASIA, *Atmos. Environ.*, 78, 291-302,
 666 <https://doi.org/10.1016/j.atmosenv.2012.03.048>, 2013.
 667 Huang, W.-R., Wang, S.-H., Yen, M.-C., Lin, N.-H., and Promchote, P.: Interannual variation of springtime biomass burning
 668 in Indochina: Regional differences, associated atmospheric dynamical changes, and downwind impacts, *J. Geophys. Res.-*
 669 *Atmos.*, 121, 10,016-010,028, 10.1002/2016jd025286, 2016a.
 670 Huang, X., Ding, A., Liu, L., Liu, Q., Ding, K., Niu, X., Nie, W., Xu, Z., Chi, X., Wang, M., Sun, J., Guo, W., and Fu, C.:
 671 Effects of aerosol–radiation interaction on precipitation during biomass-burning season in East China, *Atmos. Chem. Phys.*,
 672 16, 10063-10082, 10.5194/acp-16-10063-2016, 2016b.
 673 Huffman, G. J., Bolvin, D. T., Nelkin, E. J., Wolff, D. B., Adler, R. F., Gu, G., Hong, Y., Bowman, K. P., and Stocker, E. F.:
 674 The TRMM multisatellite precipitation analysis (TMPA): Quasi-global, multiyear, combined-sensor precipitation estimates
 675 at fine scales, *J. Hydrol.*, 8, 38-55, 10.1175/jhm560.1, 2007.
 676 Iacono, M. J., Delamere, J. S., Mlawer, E. J., Shephard, M. W., Clough, S. A., and Collins, W. D.: Radiative forcing by long-
 677 lived greenhouse gases: Calculations with the AER radiative transfer models, *J. Geophys. Res.-Atmos.*, 113,
 678 <https://doi.org/10.1029/2008JD009944>, 2008.
 679 Jacobson, M. Z.: Effects of biomass burning on climate, accounting for heat and moisture fluxes, black and brown carbon,
 680 and cloud absorption effects, *J. Geophys. Res.-Atmos.*, 119, 8980-9002, <https://doi.org/10.1002/2014JD021861>, 2014.
 681 Janjić, Z. I.: The step-mountain eta coordinate model: Further developments of the convection, viscous sublayer, and
 682 turbulence closure schemes, *Mon. Weather Rev.*, 122, 927-945, 10.1175/1520-0493(1994)122<0927:tsmecm>2.0.co;2, 1994.
 683 Jiang, Y., Yang, X.-Q., Liu, X., Qian, Y., Zhang, K., Wang, M., Li, F., Wang, Y., and Lu, Z.: Impacts of wildfire aerosols on
 684 global energy budget and climate: The role of climate feedbacks, *J. Climate*, 33, 3351-3366, 10.1175/jcli-d-19-0572.1, 2020.
 685 Kahn, R. A., Gaitley, B. J., Martonchik, J. V., Diner, D. J., Crean, K. A., and Holben, B.: Multiangle Imaging
 686 Spectroradiometer (MISR) global aerosol optical depth validation based on 2 years of coincident Aerosol Robotic Network
 687 (AERONET) observations, *J. Geophys. Res.-Atmos.*, 110, <https://doi.org/10.1029/2004JD004706>, 2005.
 688 Kaskaoutis, D. G., Nastos, P. T., Kosmopoulos, P. G., Kambezidis, H. D., Kharol, S. K., and Badarinath, K. V. S.: The
 689 Aura–OMI Aerosol Index distribution over Greece, *Atmos. Res.*, 98, 28-39, <https://doi.org/10.1016/j.atmosres.2010.03.018>,
 690 2010.

691 Koren, I., Kaufman, Y. J., Remer, L. A., and Martins, J. V.: Measurement of the effect of Amazon smoke on inhibition of
692 cloud formation, *Science*, 303, 1342-1345, 10.1126/science.1089424, 2004.

693 Lau, K. M., Kim, M. K., and Kim, K. M.: Asian summer monsoon anomalies induced by aerosol direct forcing: the role of
694 the Tibetan Plateau, *Clim. Dynam.*, 26, 855-864, 10.1007/s00382-006-0114-z, 2006.

695 Lau, W. K. M.: The aerosol-monsoon climate system of Asia: A new paradigm, *J. Meteorol. Res.-PRC.*, 30, 1-11,
696 10.1007/s13351-015-5999-1, 2016.

697 Lee, D., Sud, Y. C., Oreopoulos, L., Kim, K. M., Lau, W. K., and Kang, I. S.: Modeling the influences of aerosols on pre-
698 monsoon circulation and rainfall over Southeast Asia, *Atmos. Chem. Phys.*, 14, 6853-6866, 10.5194/acp-14-6853-2014,
699 2014.

700 Lee, H. H., and Wang, C.: The impacts of biomass burning activities on convective systems over the Maritime Continent,
701 *Atmos. Chem. Phys.*, 20, 2533-2548, 10.5194/acp-20-2533-2020, 2020.

702 Lee, W.-S., and Kim, M.-K.: Effects of radiative forcing by black carbon aerosol on spring rainfall decrease over Southeast
703 Asia, *Atmos. Environ.*, 44, 3739-3744, <https://doi.org/10.1016/j.atmosenv.2010.06.058>, 2010.

704 LeGrand, S. L., Polashenski, C., Letcher, T. W., Creighton, G. A., Peckham, S. E., and Cetola, J. D.: The AFWA dust
705 emission scheme for the GOCART aerosol model in WRF-Chem v3.8.1, *Geosci. Model Dev.*, 12, 131-166, 10.5194/gmd-
706 12-131-2019, 2019.

707 Levy, R. C., Remer, L. A., Kleidman, R. G., Mattoo, S., Ichoku, C., Kahn, R., and Eck, T. F.: Global evaluation of the
708 Collection 5 MODIS dark-target aerosol products over land, *Atmos. Chem. Phys.*, 10, 10399-10420, 10.5194/acp-10-10399-
709 2010, 2010.

710 Li, G., Chen, H., Xu, M., Zhao, C., Zhong, L., Li, R., Fu, Y., and Gao, Y.: Impacts of topographic complexity on modeling
711 moisture transport and precipitation over the Tibetan Plateau in summer, *Adv. Atmos. Sci.*, 10.1007/s00376-022-1409-7,
712 2022.

713 Li, M., Liu, H., Geng, G., Hong, C., Liu, F., Song, Y., Tong, D., Zheng, B., Cui, H., Man, H., Zhang, Q., and He, K.:
714 Anthropogenic emission inventories in China: a review, *Natl. Sci. Rev.*, 4, 834-866, 10.1093/nsr/nwx150, 2017a.

715 Li, M., Zhang, Q., Kurokawa, J. I., Woo, J. H., He, K., Lu, Z., Ohara, T., Song, Y., Streets, D. G., Carmichael, G. R., Cheng,
716 Y., Hong, C., Huo, H., Jiang, X., Kang, S., Liu, F., Su, H., and Zheng, B.: MIX: a mosaic Asian anthropogenic emission
717 inventory under the international collaboration framework of the MICS-Asia and HTAP, *Atmos. Chem. Phys.*, 17, 935-963,
718 10.5194/acp-17-935-2017, 2017b.

719 Li, Z., Lau, W. K.-M., Ramanathan, V., Wu, G., Ding, Y., Manoj, M. G., Liu, J., Qian, Y., Li, J., Zhou, T., Fan, J., Rosenfeld,
720 D., Ming, Y., Wang, Y., Huang, J., Wang, B., Xu, X., Lee, S.-S., Cribb, M., Zhang, F., Yang, X., Zhao, C., Takemura, T.,
721 Wang, K., Xia, X., Yin, Y., Zhang, H., Guo, J., Zhai, P. M., Sugimoto, N., Babu, S. S., and Brasseur, G. P.: Aerosol and
722 monsoon climate interactions over Asia, *Rev. Geophys.*, 54, 866-929, <https://doi.org/10.1002/2015RG000500>, 2016.

723 Lin, C.-Y., Zhao, C., Liu, X., Lin, N.-H., and Chen, W.-N.: Modelling of long-range transport of Southeast Asia biomass-
724 burning aerosols to Taiwan and their radiative forcings over East Asia, *Tellus B*, 66, 23733, 10.3402/tellusb.v66.23733, 2014.

725 Lin, C. Y., Hsu, H. m., Lee, Y. H., Kuo, C. H., Sheng, Y. F., and Chu, D. A.: A new transport mechanism of biomass
 726 burning from Indochina as identified by modeling studies, *Atmos. Chem. Phys.*, 9, 7901-7911, 10.5194/acp-9-7901-2009,
 727 2009.

728 Liu, L., Cheng, Y., Wang, S., Wei, C., Pöhlker, M. L., Pöhlker, C., Artaxo, P., Shrivastava, M., Andreae, M. O., Pöschl, U.,
 729 and Su, H.: Impact of biomass burning aerosols on radiation, clouds, and precipitation over the Amazon: relative importance
 730 of aerosol–cloud and aerosol–radiation interactions, *Atmos. Chem. Phys.*, 20, 13283-13301, 10.5194/acp-20-13283-2020,
 731 2020a.

732 Liu, T., Mickley, L. J., Marlier, M. E., DeFries, R. S., Khan, M. F., Latif, M. T., and Karambelas, A.: Diagnosing spatial
 733 biases and uncertainties in global fire emissions inventories: Indonesia as regional case study, *Remote Sens. Environ.*, 237,
 734 111557, <https://doi.org/10.1016/j.rse.2019.111557>, 2020b.

735 Liu, Y., Wu, G., Yu, R., and Liu, X.: Thermal adaptation, overshooting, dispersion, and subtropical anticyclone part II:
 736 Horizontal inhomogeneous heating and energy dispersion, *Chinese J. of Atmos. Sci.* (in Chinese), 25, 317-328,
 737 10.3878/j.issn.1006-9895.2001.03.03, 2001.

738 Lu, Z., Liu, X., Zhang, Z., Zhao, C., Meyer, K., Rajapakshe, C., Wu, C., Yang, Z., and Penner, J. E.: Biomass smoke from
 739 southern Africa can significantly enhance the brightness of stratocumulus over the southeastern Atlantic Ocean, *P. Natl.*
 740 *Acad. Sci. USA*, 115, 2924-2929, 10.1073/pnas.1713703115, 2018.

741 Ma, L.-M., and Tan, Z.-M.: Improving the behavior of the cumulus parameterization for tropical cyclone prediction:
 742 Convection trigger, *Atmos. Res.*, 92, 190-211, <https://doi.org/10.1016/j.atmosres.2008.09.022>, 2009.

743 Mapes, B. E.: Convective inhibition, subgrid-scale triggering energy, and stratiform instability in a toy tropical wave model,
 744 *J. Atmos. Sci.*, 57, 1515-1535, 10.1175/1520-0469(2000)057<1515:cisste>2.0.co;2, 2000.

745 Martins, J. A., Silva Dias, M. A. F., and Gonçalves, F. L. T.: Impact of biomass burning aerosols on precipitation in the
 746 Amazon: A modeling case study, *J. Geophys. Res.-Atmos.*, 114, <https://doi.org/10.1029/2007JD009587>, 2009.

747 Morrison, H., Thompson, G., and Tatarskii, V.: Impact of cloud microphysics on the development of trailing stratiform
 748 precipitation in a simulated squall line: Comparison of one- and two-moment schemes, *Mon. Weather Rev.*, 137, 991-1007,
 749 10.1175/2008mwr2556.1, 2009.

750 Myhre, G., Stordal, F., Johnsrud, M., Kaufman, Y. J., Rosenfeld, D., Storelvmo, T., Kristjansson, J. E., Berntsen, T. K.,
 751 Myhre, A., and Isaksen, I. S. A.: Aerosol-cloud interaction inferred from MODIS satellite data and global aerosol models,
 752 *Atmos. Chem. Phys.*, 7, 3081-3101, 10.5194/acp-7-3081-2007, 2007.

753 Ning, G., Wang, S., Ma, M., Ni, C., Shang, Z., Wang, J., and Li, J.: Characteristics of air pollution in different zones of
 754 Sichuan Basin, China, *Sci. Total Environ.*, 612, 975-984, <https://doi.org/10.1016/j.scitotenv.2017.08.205>, 2018.

755 Pahlow, M., Parlange, M. B., and Porté-Agel, F.: On Monin–Obukhov similarity in the stable atmospheric boundary layer,
 756 *Bound.-Lay. Meteorol.*, 99, 225-248, 10.1023/A:1018909000098, 2001.

757 [Pan, X., Ichoku, C., Chin, M., Bian, H., Darmanov, A., Colarco, P., Ellison, L., Kucsera, T., da Silva, A., Wang, J., Oda, T.,](#)
758 [and Cui, G.: Six global biomass burning emission datasets: intercomparison and application in one global aerosol model,](#)
759 [Atmos. Chem. Phys., 20, 969-994, 10.5194/acp-20-969-2020, 2020.](#)

760 Pani, S. K., Wang, S.-H., Lin, N.-H., Lee, C.-T., Tsay, S.-C., Holben, B. N., Janjai, S., Hsiao, T.-C., Chuang, M.-T., and
761 Chantara, S.: Radiative effect of springtime biomass-burning aerosols over northern Indochina during 7-SEAS/BASELInE
762 2013 campaign, Aerosol Air Qual. Res., 16, 2802-2817, 10.4209/aaqr.2016.03.0130, 2016.

763 Pani, S. K., Lin, N.-H., Chantara, S., Wang, S.-H., Khamkaew, C., Prapamontol, T., and Janjai, S.: Radiative response of
764 biomass-burning aerosols over an urban atmosphere in northern peninsular Southeast Asia, Sci. Total Environ., 633, 892-911,
765 <https://doi.org/10.1016/j.scitotenv.2018.03.204>, 2018.

766 Qin, Y., and Xie, S. D.: Spatial and temporal variation of anthropogenic black carbon emissions in China for the period
767 1980–2009, Atmos. Chem. Phys., 12, 4825-4841, 10.5194/acp-12-4825-2012, 2012.

768 Randerson, J. T., Van Der Werf, G. R., Giglio, L., Collatz, G. J., and Kasibhatla, P. S.: Global fire emissions database,
769 version 4.1 (GFEDv4), ORNL Distributed Active Archive Center, 2017.

770 Reid, J. S., Koppmann, R., Eck, T. F., and Eleuterio, D. P.: A review of biomass burning emissions part II: intensive physical
771 properties of biomass burning particles, Atmos. Chem. Phys., 5, 799-825, 10.5194/acp-5-799-2005, 2005.

772 Requia, W. J., Amini, H., Mukherjee, R., Gold, D. R., and Schwartz, J. D.: Health impacts of wildfire-related air pollution in
773 Brazil: a nationwide study of more than 2 million hospital admissions between 2008 and 2018, Nat. Commun., 12, 6555,
774 10.1038/s41467-021-26822-7, 2021.

775 Sakaeda, N., Wood, R., and Rasch, P. J.: Direct and semidirect aerosol effects of southern African biomass burning aerosol,
776 J. Geophys. Res.-Atmos., 116, <https://doi.org/10.1029/2010JD015540>, 2011.

777 Shi, Y., Sasai, T., and Yamaguchi, Y.: Spatio-temporal evaluation of carbon emissions from biomass burning in Southeast
778 Asia during the period 2001–2010, Ecol. Model., 272, 98-115, <https://doi.org/10.1016/j.ecolmodel.2013.09.021>, 2014.

779 Torres, O., Tanskanen, A., Veihelmann, B., Ahn, C., Braak, R., Bhartia, P. K., Veefkind, P., and Levelt, P.: Aerosols and
780 surface UV products from Ozone Monitoring Instrument observations: An overview, J. Geophys. Res.-Atmos., 112,
781 <https://doi.org/10.1029/2007JD008809>, 2007.

782 [Takeishi, A., and Wang, C.: Radiative and microphysical responses of clouds to an anomalous increase in fire particles over](#)
783 [the Maritime Continent in 2015, Atmos. Chem. Phys., 22, 4129-4147, 10.5194/acp-22-4129-2022, 2022.](#)

784 Tummon, F., Solmon, F., Lioussé, C., and Tadrass, M.: Simulation of the direct and semidirect aerosol effects on the
785 southern Africa regional climate during the biomass burning season, J. Geophys. Res.-Atmos., 115,
786 <https://doi.org/10.1029/2009JD013738>, 2010.

787 Wang, J., Jiang, Q., You, Y., Rao, X., Sheng, L., Gui, H., Hua, C., and Zhang, B.: Effects of biomass burning aerosol in
788 Southeast Asia on haze and precipitation over China, Meteor. Mon. (in Chinese), 47, 348-358, 2021.

789 Wiedinmyer, C., Akagi, S. K., Yokelson, R. J., Emmons, L. K., Al-Saadi, J. A., Orlando, J. J., and Soja, A. J.: The Fire
790 INventory from NCAR (FINN): a high resolution global model to estimate the emissions from open burning, *Geosci. Model*
791 *Dev.*, 4, 625-641, 10.5194/gmd-4-625-2011, 2011.

792 Wu, G., and Liu, Y.: Thermal adaptation, overshooting, dispersion, and subtropical anticyclone part I: Thermal adaptation
793 and overshooting, *Chinese J. of Atmos. Sci.* (in Chinese), 24, 433-446, 10.3878/j.issn.1006-9895.2000.04.01 2000.

794 Wu, G., Li, Z., Fu, C., Zhang, X., Zhang, R., Zhang, R., Zhou, T., Li, J., Li, J., Zhou, D., Wu, L., Zhou, L., He, B., and
795 Huang, R.: Advances in studying interactions between aerosols and monsoon in China, *Sci. China Earth Sci.*, 59, 1-16,
796 10.1007/s11430-015-5198-z, 2016.

797 Yadav, I. C., Linthoingambi Devi, N., Li, J., Syed, J. H., Zhang, G., and Watanabe, H.: Biomass burning in Indo-China
798 peninsula and its impacts on regional air quality and global climate change-a review, *Environ. Pollut.*, 227, 414-427,
799 <https://doi.org/10.1016/j.envpol.2017.04.085>, 2017.

800 Yang, Q., Zhao, T., Tian, Z., Kumar, K. R., Chang, J., Hu, W., Shu, Z., and Hu, J.: The cross-border transport of PM_{2.5} from
801 the Southeast Asian biomass burning emissions and its impact on air pollution in Yunnan Plateau, Southwest China, *Remote*
802 *Sens.-Basel*, 14, 1886, 2022a.

803 Yang, S., Lau, W. K. M., Ji, Z., Dong, W., and Yang, S.: Impacts of radiative effect of pre-monsoon biomass burning
804 aerosols on atmospheric circulation and rainfall over Southeast Asia and southern China, *Clim. Dynam.*, 10.1007/s00382-
805 021-06135-7, 2022b.

806 Zaveri, R. A., and Peters, L. K.: A new lumped structure photochemical mechanism for large-scale applications, *J. Geophys.*
807 *Res.-Atmos.*, 104, 30387-30415, <https://doi.org/10.1029/1999JD900876>, 1999.

808 Zaveri, R. A., Easter, R. C., Fast, J. D., and Peters, L. K.: Model for simulating aerosol interactions and chemistry
809 (MOSAIC), *J. Geophys. Res.-Atmos.*, 113, <https://doi.org/10.1029/2007JD008782>, 2008.

810 Zhang, Y., Fu, R., Yu, H., Qian, Y., Dickinson, R., Silva Dias, M. A. F., da Silva Dias, P. L., and Fernandes, K.: Impact of
811 biomass burning aerosol on the monsoon circulation transition over Amazonia, *Geophys. Res. Lett.*, 36,
812 <https://doi.org/10.1029/2009GL037180>, 2009.

813 Zhao, J., Ma, X., Wu, S., and Sha, T.: Dust emission and transport in Northwest China: WRF-Chem simulation and
814 comparisons with multi-sensor observations, *Atmos. Res.*, 241, 104978, <https://doi.org/10.1016/j.atmosres.2020.104978>,
815 2020.

816 Zhou, Y., Yan, H., and Luo, J.-J.: Impacts of amazon fire aerosols on the subseasonal circulations of the mid-high latitudes,
817 *Front. Earth Sci.*, 8, 10.3389/feart.2020.609554, 2021.

818 Zhu, A., Xu, H., Deng, J., Ma, J., and Li, S.: El Niño–Southern Oscillation (ENSO) effect on interannual variability in spring
819 aerosols over East Asia, *Atmos. Chem. Phys.*, 21, 5919-5933, 10.5194/acp-21-5919-2021, 2021.

820